1	Emergent Feedbacks Between Progressive Serpentinization, Interface
2	Weakening, and Subduction Rates
3	
4	R. K. Stoner <sup>1</sup> , A. F. Holt <sup>1*</sup> , G. S. Epstein <sup>1,2</sup> , V. E. Guevara <sup>3</sup> , and C. B. Condit <sup>2</sup>
5	
6	<sup>1</sup> Rosenstiel School of Marine, Atmospheric, and Earth Science, University of Miami, Miami, FL, 33149, USA
7	<sup>2</sup> Department of Earth and Space Sciences, University of Washington, Seattle, WA, 98195, USA.
8	<sup>3</sup> Geology Department, Amherst College, Amherst, MA, 01002, USA.
9	
10	*Corresponding author: Adam F. Holt (aholt@miami.edu)

#### 12 **Key Points:**

11

13

- Dynamic subduction models capture feedbacks between thermal state, mantle wedge serpentinization, interface weakening, and plate speeds.
- Sediment lubricates the plate interface indirectly by providing water that reacts with the mantle wedge to produce weak serpentinite.
- Serpentinization promotes faster plate speeds, especially after early subduction and
   sufficient serpentinite accumulation.

#### Abstract

19

20

21

22

23

24

25

26

27

28

29

30

31

32

33

34

35

36

37

38

39

40

41

42

43

44

45

46

47

48

During subduction, the downgoing oceanic crust is exposed to high temperatures in the mantle wedge, causing volatile-bearing minerals to break down and release hydrous fluids into the forearc. These fluids percolate upwards, reacting with the mantle wedge to form hydrated ultramafic lithologies, including serpentinite. To accurately track the fate and impact of water on the forearc, we develop time-dependent models that self-consistently capture both serpentinite ingrowth and the associated rheological weakening of the plate interface. Unlike many subduction models that investigate forearc serpentinization that prescribe plate velocities, geometries, or steady-state conditions, our approach allows plates to evolve dynamically without predefined velocities or geometries. During subduction infancy, serpentinite accumulates rapidly. As subduction matures, serpentinite ingrowth decreases, and more serpentinite is also dragged downwards by the slab. To elucidate links between subduction dynamics and serpentinization, we consider variations in serpentinite strength and hydration state of the incoming plate. Subducting fully water-saturated sediments yields ~ 3× greater forearc serpentinite than within the moderately hydrated reference case. This produces a weaker interface and, in turn, subduction zone convergence rates that are  $\sim$  40% higher than in an endmember case with anhydrous sediment. A lower serpentinite strength also produces higher convergence rates, despite more downdragging of serpentinite from the forearc. We find that hydrous sediments not only lubricate the interface directly by weakening it, as previously suggested, but also by dehydrating and releasing water that produces weak serpentinite in the mantle wedge, with such feedbacks only able to be captured within fully coupled dynamic models.

# **Plain Language Summary**

We develop and analyze computer models of subduction where plate forces and speeds can change freely and where water movement is tracked. Water moving upwards from the plate interface during subduction forms weak rocks called serpentinites. We find these weak serpentinites can lubricate the interface between plates and speed up subduction over time. This is also important because previous research proposed that sediments may change subduction speeds. Instead, sediments release water that is needed for weak serpentinites to form that could also lubricate the interfaces of subducting plates.

#### 1 Introduction

The mechanical and compositional properties of the plate interface underpin a range of subduction behaviors, including deformation (Shreve & Cloos, 1986; Behr & Bürgmann, 2021), rock exhumation (Gerya et al., 2002; Agard et al., 2018), deep mantle hydration (Rüpke et al., 2004; Faccenda et al., 2012; Magni et al., 2014), and volatile budgets in the mantle wedge (Ito et al., 1983; Schmidt & Poli 1998; Iwamori, 2007; Hacker, 2008; van Keken et al., 2011). Volatiles are liberated from the downgoing plate, migrate upwards, and, depending on the fluid composition and pressure-temperature (*P-T*) conditions, may be bound in weak hydrous lithologies, such as serpentinite (Peacock, 1990; Hyndman & Peacock, 2003; Abers et al., 2017; Epstein et al., 2024). Moreover, subduction zones are dynamic systems, and therefore both *P-T* conditions and associated fluid release and storage change over time. To investigate these interrelated processes, we develop numerical subduction models to estimate the impacts of dehydration and/or hydration patterns on large-scale subduction zone evolution.

Previous studies have made strides in predicting slab water release and mantle wedge hydration by coupling the thermal fields from time-invariant, kinematically driven subduction models—characterized by fixed slab dips and convergence rates—with metamorphic phase equilibria calculations (Hyndman & Peacock, 2003; Hacker, 2008; van Keken et al., 2011; Abers et al., 2017). However, both geological (Platt, 1975; Cloos, 1985; Agard et al., 2018; Dragovic et al., 2020) and numerical studies (Peacock, 1990; Molnar & England, 1990; Wang et al., 1995) predict that slab temperatures, and hence dehydration patterns, evolve over time. These thermal changes create transients in mantle wedge hydration and dehydration, which time-invariant models cannot capture. For example, rapid changes in slabtop temperatures can arise due to time-dependent kinematic properties that make up the "thermal parameter" (e.g., Kirby et al., 1996; van Keken et al., 2011), such as convergence rates, which can evolve even over million-year timescales (Faccenna et al., 2001; Sdrolias & Müller, 2006). These changes are self-consistently captured in "dynamic" subduction models, where plate forces and velocities are allowed to evolve freely without external forcing. These models self-consistently produce a highly time-dependent slab thermal structure (e.g., Kincaid & Sacks, 1997; Billen & Arredondo, 2018) and hence timedependent water release (Holt & Condit, 2021; Zhou & Wada, 2021). Fluctuations in water

release also affect water storage: a postprocessing of Holt and Condit's (2021) dynamic subduction thermal models revealed that slab water release and water storage in mantle wedge serpentinites almost always exceed those predicted by fixed-geometry, constant-velocity subduction models (Abers et al., 2017) because dynamic models capture the hotter, earlier stages of subduction (Epstein et al., 2024). However, in a dynamic context, the release and storage of water is also likely to impact the slab evolution itself, because weak hydrous minerals accumulating near the plate interface influence the mechanical and rheological properties of the interface.

80

81

82

83

84

85

86

87

88

89

90

91

92

93

94

95

96

97

98

99

100

101

102

103

104

105

106

107

108

109

110

While previous studies have incorporated time-dependent hydration of the mantle wedge and associated serpentinite ingrowth, they have typically prescribed plate speeds and/or subduction zone geometries. These assumptions, in turn, neglect the dynamic evolution of subduction zone properties, such as convergence rate and dip, and hence the resulting impact of changes in these kinematic properties on slab and wedge temperatures, dehydration/hydration, and vice versa. Such studies have successfully captured the impacts of serpentinization in contexts such as high/ultra-high pressure rock exhumation (Gerya et al., 2002; Gerya & Stöckhert, 2006), arc magmatism (Gorczyk et al., 2007; Nikolaeva et al., 2008; Gerya & Meilick, 2011), mantle wedge dynamics (Wada et al., 2008; Li et al., 2019; Kerswell et al., 2021), and steady-state water budgets (Wada et al., 2012; Abers et al., 2017). Other studies have illuminated some of the feedbacks between serpentinization and large-scale subduction using models implementing wedge hydration and milder kinematic prescriptions, such as prescribed boundary conditions for part of the model duration (Li et al., 2019; Balázs et al., 2022), or prescribed velocities on only one of the two plates (Arcay et al., 2005, 2006). Some notable exceptions include the studies of Nakao et al. (2016, 2018), which did employ dynamic models to explore the significant impact of wedge hydration on subduction properties, such as convergence rates and slab dips, but focused on hydrous weakening in a generalized sense (i.e., not serpentinite-specific). Ritter et al. (2024) also implemented wedge hydration, and in this case serpentinization, in the context of dynamically-evolving subduction but with a specific focus on subduction initiation. However, taken together, most previous subduction modeling studies have thus integrated only specific feedbacks related to slab dehydration and mantle wedge serpentinization within kinematically-driven models, or, within dynamic models, explored generic fluid-related

mantle weakening and/or focused on specific phases of subduction. Here, we therefore conduct a comprehensive examination of the interplay between forearc hydration and serpentinization, interface properties, and their combined influence on dynamically evolving subduction properties.

111

112

113

114

115

116

117

118

119

120

121

122

123

124

125

126

127

128

129

130

131

132

133

134

135

136

137

138

139

140

141

One example of how serpentinization may impact large-scale subduction is by modifying the strength of the plate interface, which, in turn, affects the subduction zone force balance and hence plate velocities. Such feedbacks between slab behavior, such as plate speeds, and variable interface strength have been explored within fully dynamic models for interfaces with uniform lithologies at the slabtop (Čížková & Bina, 2013; Behr et al., 2022). For example, weak subducting materials, including sediment (Shreve & Cloos, 1986; Lamb, 2006; Behr & Becker, 2018) and altered oceanic crust (Kimura & Ludden, 1995), can impact subduction zone plate speeds by reducing the net subducting-resisting shear stress exerted on the slab by the interface (Conrad & Hager, 1999). However, in contrast to a potentially steady input of sediment or oceanic crust, weak hydrous minerals, such as serpentine (Moore & Lockner, 2004; Wada & Wang, 2009) or talc (Horn & Deere, 1962; Boneh et al., 2023), accumulate in the mantle wedge over time as hydrous fluids are released from the downgoing slab. These minerals have been shown to weaken the plate interface in models with hydration of the mantle wedge (Arcay et al., 2005; Gerya et al., 2008; Nakao et al., 2016, 2018). Therefore, we expect serpentinite accumulation in the mantle wedge to cause a time-dependent feedback loop with subduction kinematics, such as plate speeds, because serpentine stability in the mantle wedge is highly dependent on the time-evolving P-T conditions. These conditions are modulated by advection driven by plate speeds, which are, in turn, influenced by the strength of weak materials at the plate interface, including serpentinite. Thus, examining feedbacks between slab thermal structure, serpentinization, and plate dynamics requires the coupling of temperaturedependent dehydration and hydration with freely evolving model subduction zones.

To reveal the scope of emergent feedbacks between serpentinization and large-scale subduction zone evolution, we present dynamic models of subduction with weak serpentinite ingrowth near the plate interface. We isolate the impacts of slab dehydration, wedge hydration via serpentinization, and associated strength changes of the plate interface by examining numerical models with varying interface yielding properties and hydration

states of the downgoing slab crust. By simulating serpentinite formation and its feedback on temperature, water release, and plate interface lubrication, these models directly capture and quantify time-dependent subduction zone strength and dynamics.

#### 2 Materials and Methods

We develop 2-D ocean-ocean subduction models using the ASPECT finite element code (ASPECT v2.5.0-pre; Kronbichler et al., 2012; Heister et al., 2017; Rose et al., 2017; Gassmöller et al., 2018; Bangerth et al., 2023). We solve for the conservation of momentum, mass, and energy, respectively. The incompressible Boussinesq approximation is used for mass conservation, and we do not incorporate radioactive or shear heating:

151 1. 
$$-\nabla \cdot 2\eta \dot{\varepsilon}(v) + \nabla p = \rho g$$

152 2. 
$$\nabla \cdot v = 0$$

153 3. 
$$\rho C_p \left( \frac{\partial T}{\partial t} + v \cdot \nabla T \right) - k \nabla^2 T = 0$$

Where  $\eta$  is viscosity,  $\dot{\varepsilon}$  is strain rate, v is velocity, p is the total pressure,  $\rho$  is density, and g is gravitational acceleration. In the heat conservation equation  $C_p$  is the specific heat capacity, T is temperature, and k is thermal conductivity. Individual lithologies are represented by compositional fields that are advected by the flow field. Advection of these compositional fields is treated by an additional advection equation (Equation 4) for each field c to the preceding equations (Equation 1-3):

160 4. 
$$\frac{\partial c_i}{\partial t} + v \cdot \nabla c_i = q_i$$

A source reaction term q is used to update compositional quantities, such as the ingrowth of serpentinite.

We consider an initially 100-million-year-old oceanic plate subducting below a younger, 10-million-year-old overriding plate to ensure self-sustained subduction (Figure 1). Spreading centers are located 500 km from either boundary of the domain at the margins of both the subducting plate and overriding plate. An initial curved section of the subducting plate is included that extends to a depth of 50 km and to 145 km inboard of the trench. The

model domain dimensions are  $5800 \times 1450$  km. All other associated parameters are listed in Table 1 and Table S1. `

The models are dynamic, and plate forces and geometries are allowed to evolve freely. In terms of thermal structure and (non-interface) mechanical properties, the models are similar to those of Holt and Condit (2021). However, unlike in this previous work, the present models contain a free surface with surface diffusion at the upper boundary. This free surface is allowed to isostatically equilibrate for 100 timesteps prior to the main 50 million year-long model run (Figure 1). A diffusion coefficient of  $10^{-7}$  m²/s is used to prevent extreme topographic gradients and hence increase numerical stability (e.g., Rose et al., 2017). Except for this free surface upper boundary, free-slip boundaries are enforced elsewhere. A constant mantle potential temperature of 1421°C is used (GDH1 plate cooling model: Stein & Stein, 1992). Constant temperatures are enforced at the bottom (1421°C) and top (0 °C) of the domain. Insulated (no heat flux) boundary conditions are enforced on the left and right sides of the domain.

ASPECT's adaptive mesh refinement (AMR) functionality is used to locally increase model resolution in regions with high strain rates, high temperatures, or within regions containing threshold quantities of the lithologies (or compositions, i.e. Equation 4) that make up the plate interface region. Refinement levels are chosen so that there is a minimum resolution of  $\sim 230$  km and a maximum resolution of  $\sim 1.3$  km (e.g., within the plate interface). We also set the resolution near the 660 km discontinuity to have a grid size of  $\sim 2.6$  km. In the reference model, the initial number of degrees of freedom is  $\sim 2,900,000$ , and the final number of degrees of freedom at the end of the run, after increasing amounts of mesh refinement, is  $\sim 9,400,000$ .

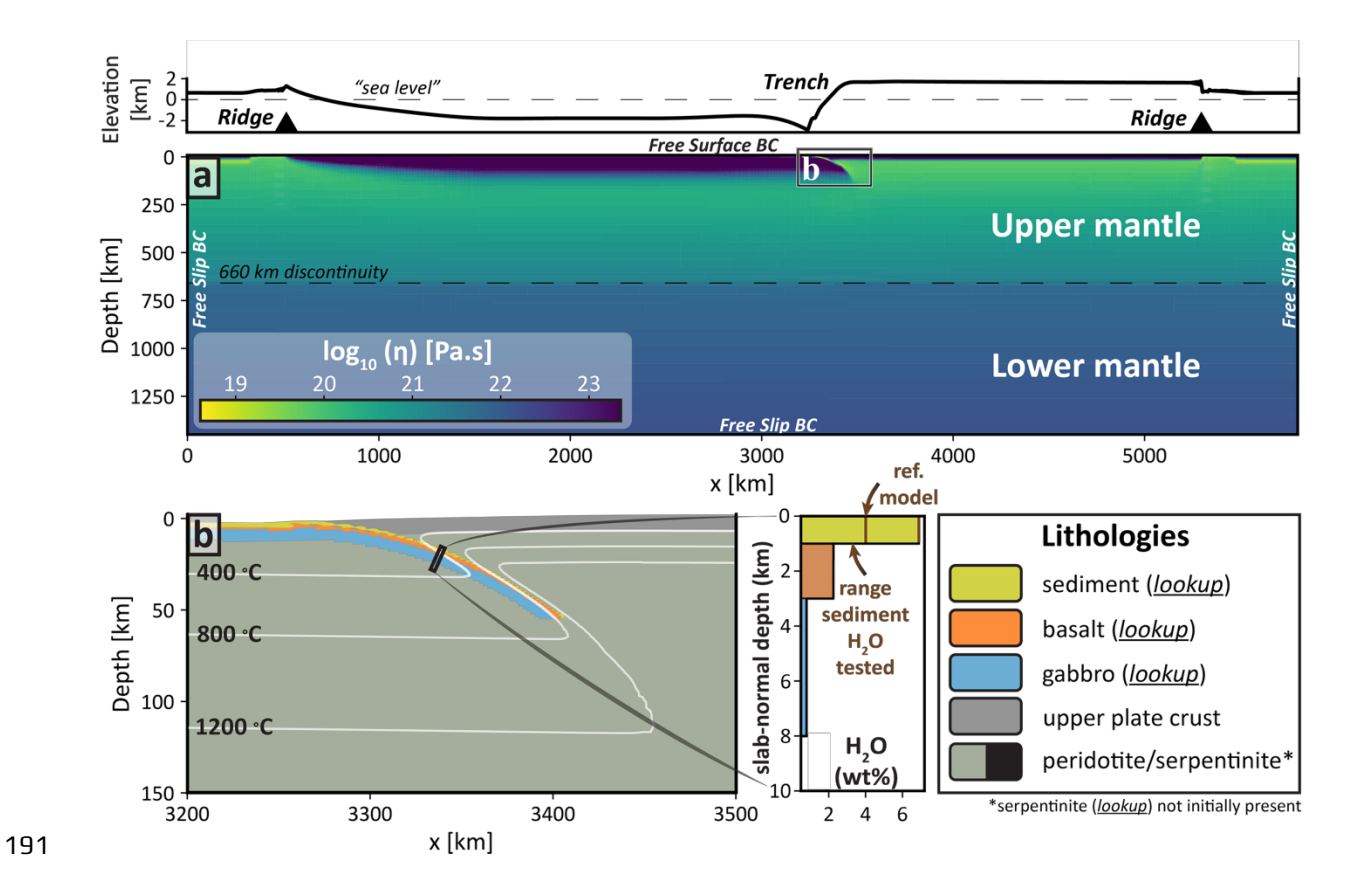


**Figure 1.** Model set-up showing the initial viscosity field and initial, isostatically equilibrated, topography (a) with a zoom-in of the subduction interface region (b). The lithologies/compositions of the downgoing crust are also shown, with thicknesses and the range of explored sediment H<sub>2</sub>O concentrations (see Methods Sections 2.1-2.2). As illustrated, some compositions use lookup tables to assign rheology and density (see Table 1).

# 2.1 Phase stability

Our model crust is constructed as a simplified version of the oceanic crust described in Jarrard (2003) and overlain by pelagic sediment with a composition from Hacker (2008). The crust is composed of, in order of increasing depth away from the slabtop, 1 km of pelagic sediment, 2 km of metabasalt, and 5 km of metagabbro (Figure 1b). Assuming a 100 Myr old oceanic crust, the metabasalt initial H<sub>2</sub>O content is calculated as an average of the H<sub>2</sub>O content of 300 m of upper volcanic extrusives (6.04 wt. %), 300 m of lower extrusives (4.1 wt. %), and 1600 m of sheeted dykes (1.76 wt. %) for an H<sub>2</sub>O content of 2.3 wt. % distributed homogeneously throughout the 2 km of slab upper crust. The metagabbro has 0.79 wt. % H<sub>2</sub>O, while the pelagic sediment has 6.89 wt. % H<sub>2</sub>O because we infer it is fully saturated. However, to explore the impact of variable H<sub>2</sub>O inputs, we examine a range of sediment H<sub>2</sub>O concentrations relative to this reference value (Figure 1b). No initial pore fluid

is included for any of the crust; all  $H_2O$  is initially mineralogically bound (Table 1). Hydration of abyssal serpentinite is not considered because abyssal serpentinite dehydration occurs beyond serpentinite stability in the wedge, as expected given that slab interiors are cooler than slab tops (Epstein et al., 2024), though km-scale layers of abyssal serpentinites with very low density may resist subduction (Nakao et al., 2018).

Phase equilibria modelling is used to track the stable mineral assemblage in the various slab lithologies as a function of pressure-temperature (P-T) conditions. Density and bound water content for all crustal compositions are determined directly from the phase equilibria results, and viscosities are calculated within ASPECT using flow laws associated with the dominant calculated mineral modes (see Section 2.4). Fluid released during metamorphic dehydration reactions (assumed to be pure H<sub>2</sub>O) is determined by monitoring changes in the bound water content of the mineral assemblage during prograde metamorphism, similar to previous studies (van Keken et al., 2011; Wada et al., 2012; Abers et al., 2017; Condit et al., 2020; Epstein et al., 2024). Once free water is produced, it is tracked as described in the following section. We use "water" throughout the text interchangeably with H<sub>2</sub>O even though such fluid may be supercritical in part of the domain. Phase equilibria modeling and the production of data tables used by ASPECT were performed using Perple\_X version 7.0.1 (Connolly, 2005). All thermodynamic calculations were carried out in the system Na<sub>2</sub>O-CaO-K<sub>2</sub>O-FeO-MgO-Al<sub>2</sub>O<sub>3</sub>-SiO<sub>2</sub>-H<sub>2</sub>O. We use the thermodynamic database of Holland and Powell (2011) and Pitzer and Sterner (1994) for the fluid equation of state. Solid solution models for all calculations are provided in the Supporting Information (Table S2).

#### 2.2 H<sub>2</sub>O Transport

208

209

210

211

212

213

214

215

216

217

218

219

220

221

222

223

224

225

226

227

228

229

230

231

232

233

234

235

236

237

Although the mantle wedge is not initially hydrated, the hydrated crust from the downgoing plate encounters relatively hotter conditions in the mantle wedge, causing the crust, including the pelagic sediment, to progressively dehydrate and release free  $H_2O$ , or water. In our models, the free  $H_2O$  is stored and transported throughout the domain as a compositional field (Equation 4), i.e., in addition to those representing crustal lithologies and serpentinite. Figure 2 shows a flowchart depicting the treatment of this water release, transport, and storage in the model. After the  $O^{th}$  timestep, mineral-bound  $H_2O$  is assigned

in all source lithologies where water is expected to be present (i.e., following Figure 1b). At each subsequent timestep, the mineral-bound  $H_2O$  content for each lithology is recalculated using lookup tables created from Perple\_X phase equilibria modeling results. This updated, mineral-bound  $H_2O$  content is then compared to the mineral-bound  $H_2O$  content of the previous step. If the new bound  $H_2O$  content is lower than the preceding timestep, then water must be released: the difference becomes the amount of the free  $H_2O$  phase present in the system that is produced by the metamorphic breakdown of hydrous minerals. If no  $H_2O$  release occurs, then no dehydration takes place.

Treating free  $H_2O$  and other lithologies as a continuum and not as particles means that, in each model cell, the associated compositions can be less than unity, and hence individual compositions in the crustal column can numerically diffuse into each other (Kronbichler et al., 2012). During the dehydration calculations we therefore scale each bound  $H_2O$  amount for the magnitude of each composition (from 0-100%) within a given cell to prevent over or under-prediction of the  $H_2O$  content.

Free  $H_2O$  is, for simplicity, advected vertically upward at a constant rate of 10 cm/yr (e.g., Gerya et al., 2002; Gorczyk et al., 2007). In practice, this is implemented by modifying the ASPECT "plug-in" of Douglas et al. (2023) that adds two-phase (Darcy) flow to ASPECT. Here, instead of solving for the fluid velocity, we set the velocity at a constant value in the plug-in.

Free H<sub>2</sub>O may interact with the mantle wedge in three ways: a) if the temperature is above the calculated wet solidus (Katz et al., 2003) then all the free fluid is assumed to be absorbed into the melts, which can readily accept >10 wt. % H<sub>2</sub>O (Hamilton et al., 1964; Mitchell et al., 2017; Gavrilenko et al., 2019). Melt migration and the effect of melt on viscosity are not modeled: a melt region is calculated purely to be consistent with H<sub>2</sub>O being incorporated into melts, removing the associated free H<sub>2</sub>O, and hence preventing extensive serpentinization of the base of the overriding plate in the "arc region;" b) If the temperature is below that of the solidus yet above that of serpentinization stability, free H<sub>2</sub>O continues to be advected upwards but weakens the surrounding mantle by a factor of 100. This mimics the weaker rheology of a hydrated peridotite, which has a lower viscosity than dry olivine aggregates as a proxy for peridotite (Hirth & Kohlstedt, 2003). c) If the free H<sub>2</sub>O is in the mantle and within the serpentinite stability field, it is bound within a "serpentinite

compositional field." Free  $H_2O$  is not allowed to react with the overriding plate crust. Any free  $H_2O$  that reaches the Earth's surface is removed from the model.

Serpentinite can also be dragged downwards to *P-T* conditions outside of serpentinite stability. While the resulting deserpentinization is not tracked directly, if any such material in the serpentinite field exits the region of serpentinite stability, then the background olivine flow law and peridotite density are re-imposed. For clarity, we use the terms *cumulative serpentinite* to denote the "serpentinite" compositional field, which includes both currently stable serpentinite and mantle material that has deserpentinized, and the term *instantaneous serpentinite*, which refers to any serpentinite that is currently stable as serpentinite.

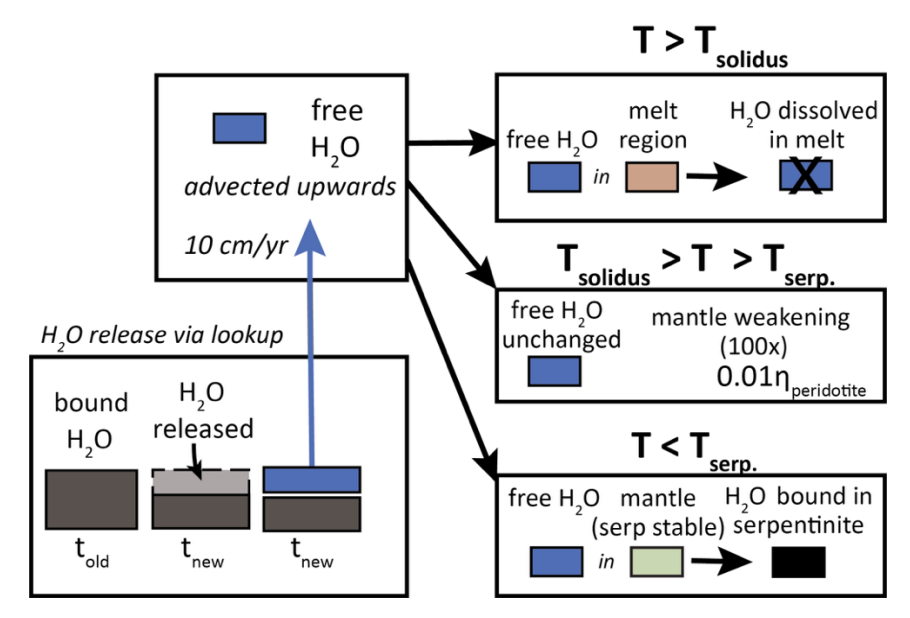


Figure 2. Flowchart illustrating our implementation of water release, transport, and storage. Bound  $H_2O$  is calculated with lookups created from the outputs of Perple\_X phase equilibria calculations. At each timestep, new and old  $H_2O$  contents are calculated, and the remaining  $H_2O$  is transformed into a "free  $H_2O$ " phase, which percolates upward at 10 cm/yr. If free  $H_2O$  interacts with the mantle wedge it: a) is absorbed into melts if the temperature is above the calculated wet solidus  $H_2O$  (Katz et al., 2003), b) continues to be advected upwards, but causes a weakening of the surrounding mantle by 100x, if the temperature is between the temperature of the solidus and serpentinization, c) is bound within a "serpentinite field" if serpentinite is stable based on the associated lookup table.

## 2.3 Rheology

We first describe the overarching equations governing rheology, including yielding and creep deformation, within all model compositions. In subsequent subsections, we detail

the parameters used for specific compositions. Overall, we adopt a composite flow law, with diffusion creep, dislocation creep, and pseudo-plastic yielding (Glerum et al., 2018) for the background lithosphere and mantle (i.e., outside of the plate interface materials and any serpentinite). Both diffusion and dislocation creep mechanisms are assigned viscosities following the idealized flow law:

5. 
$$\eta_{creep} = A^{\frac{-1}{n}} \dot{\varepsilon}_{II}^{\frac{1-n}{n}} f_{H_2O}^r exp\left(\frac{Ea+PV}{nRT}\right)$$

where A is the creep prefactor, n is the stress exponent (1 for olivine diffusion creep;  $\sim 3.5$  for olivine dislocation creep),  $\dot{\varepsilon}_{II}$  is the second invariant of the deviatoric strain rate, E is the activation energy, V is the activation volume, R is the ideal gas constant, and T is the temperature (Table 1). An exponential weakening term is also used for crustal rheologies whose P-T conditions intersect the solidus, which only occurs early in the model evolution (Figure S1). Despite the assumption of incompressibility in our conservation equations (Equations 1-2), we add a 0.3 °C/km adiabatic temperature gradient to temperatures used in the creep formulation.

We also incorporate pseudo-plastic yielding in the form of a "plastic" viscosity,  $\eta_{plastic}$ . The process of forming brittle fractures at the scale seen in nature, on the submeter scale or outcrop scale (e.g., Rowe et al., 2013), is computationally infeasible in the current models. Furthermore, multiple strain mechanisms, brittle, semi-brittle, and viscous may be operating concurrently. All such deformation processes tend to produce highly localized regions of shear in regions such as the bending portion of the subducting lithosphere (e.g., Ranero et al., 2003). We therefore subsume all such mechanisms into a plastic component using a 2-D Drucker-Prager criterion to prescribe a yield stress,  $\sigma_{\gamma}$ :

6. 
$$\sigma_{v} = C\cos(\varphi) + \sin(\varphi)P$$

Where C is the cohesion, P the pressure, and  $\varphi$  is the friction angle. Furthermore, an array of studies has already shown that pore-fluid pressure along the subduction interface is likely high during shear (Audet & Bürgmann, 2014; Peacock et al., 2011; Condit & French, 2022). We therefore use an "effective friction" coefficient that is meant to encapsulate the

effects of pore-fluid overpressure, which weakens the interface. We therefore recast Equation 6 as:

322 
$$\sigma_{v} = \mu_{eff} P + C_{0}$$

323 8. 
$$\mu_{eff} = (1 - \lambda)\mu$$

Where  $C_0$  is a modified cohesion that includes the friction angle term, and  $\lambda$  is a pore fluid pressure coefficient. The plastic viscosity is then computed as a function of the yield stress and second invariant of the deviatoric strain rate:

$$9. \eta_{plastic} = \frac{\sigma_y}{2\dot{\epsilon}_{II}}$$

Viscosities associated with the different rheological mechanisms are then harmonically averaged to generate the model (or "composite") viscosity:

330 10. 
$$\frac{1}{\eta_{composite}} = \frac{1}{\eta_{diff}} + \frac{1}{\eta_{disl}} + \frac{1}{\eta_{plastic}}$$

The subscripts "diff," "disl," and "plastic" refer to diffusion creep, dislocation creep, and plastic viscosity components, respectively. If a model grid cell contains more than one composition (e.g., basalt and sediment), the respective composite viscosities are averaged using a geometric mean. All rheological parameters for all compositions are detailed in the following three sub-sections and listed in Table 1.

7	7	_
ר	ר	п
_	_	_

Composition	Flow law <sup>a</sup>	A	n	Ea	r	V	τ <sub>0</sub> (LTP) <sup>b</sup>	p (LTP) <sup>b</sup>	q (LTP) <sup>b</sup>	melt	C <sub>0</sub>	µ <sub>eff</sub>	Initial H₂O	Reference density
		[Pa <sup>-n</sup> .s <sup>-1</sup> ]	-	[kJ/mol]	-	[cm³mol-1]	[GPa]	-	-	-	[MPa]	_	[wt. %]	[kg/m³]
sediment	wet quartz <sup>d</sup>	6.31×10 <sup>-36</sup>	4	135	1	0	-	-	-	-	1	0.02	6.89	lookup
metabasalt	wet quartz <sup>d</sup>	6.31×10 <sup>-36</sup>	4	135	1	0	-	-	-	-	1	0.04	2.32	lookup
	amphibolitee	6.94×10 <sup>-27</sup>	3.7	244	0	0	-	-	-	27				
	eclogite <sup>f</sup>	1.99×10 <sup>-18</sup>	3.5	403	0	27.2	-	-	-	27				
metagabbro	wet quartz <sup>d</sup>	6.31×10 <sup>-36</sup>	4	135	0	0	-	-	-	-	20	0.04	0.79	lookup
	amphibolite <sup>e</sup>	6.94×10 <sup>-27</sup>	3.7	244	1	0	-	-	-	27				
	eclogite <sup>f</sup>	1.99×10 <sup>-18</sup>	3.5	403	0	27.2	-	-	-	27				
serpentinite	serpentinite <sup>b,c</sup>	4.37×10 <sup>-22</sup>	2	86.3	-	_	2.42	1	1.18	-	1	0.01- 0.06	_	lookup

mantle	dry olivine (disl. creep) <sup>g</sup>	9.15×10 <sup>-20</sup>	3.5	540	0	12	_	_	_	_	20	0.36	0	3300
	dry olivine (diff. creep) <sup>g</sup>	9.6×10 <sup>-12</sup>	1	300	0	4	_	_	_	_				
overriding plate oceanic crust	same as mantle	-	_	_	-	_	_	-	-	-		0.36	0	2800
yielding region	same as mantle	_	-	_	-	_	_	-	-	-		0	0	3300
lower mantle	20× olivine diff.	4.8x10 <sup>-13</sup>	1	300	0		_	_	_	_		0.36	0	3300

\*Equation 5; \*Burdette & Hirth (2022) and Fildes & Billen (2025); \*Equation 12; \*Hirth et al. (2001); \*Hacker & Christie (1990); \*Thang & Green (2007); \*Karato & Wu (1993)

**Table 1.** Model parameters associated with individual compositions.

## 2.3.1 Mantle Rheology

The viscous component of the background mantle deforms via a combination of diffusion and dislocation creep, with activation volumes and energies corresponding to those of dry olivine (Karato & Wu, 1993; Table 1). Diffusion and dislocation prefactors are set to produce a composite viscosity of  $2.5\times10^{20}$  Pa s (i.e.,  $\eta_{diff} = \eta_{disl} = 5\times10^{20}$  Pa s) at a reference strain rate of  $10^{-14}$  s<sup>-1</sup>, the background mantle temperature, and lithostatic pressures corresponding to 330 km depth (cf. Billen & Hirth, 2005). These values result in sub-lithospheric deformation that is dominated by dislocation creep down to depths of  $\sim$  250 km, as is broadly consistent with constraints from seismic anisotropy (Becker, 2006; Podolefsky et al., 2004). A weakening factor of  $100\times$  is imposed in the mantle in regions with free H<sub>2</sub>O to mimic the weaker rheology of hydrated peridotites (i.e., an additional 0.01 prefactor added to Equation 5), which have lower viscosities than the dry olivine used to approximation peridotite (Hirth & Kohlstedt, 2003).

At depths greater than 660 km, the lower mantle is allowed to deform only via diffusion creep, with the lower mantle diffusion creep prefactor set to produce a viscosity 20 times that of upper mantle diffusion creep. The thickness of the transition to the lower mantle is 1 km. As outlined, our yield stress formulation considers both a friction coefficient  $\mu$ , as traditionally measured in rock deformation experiments, and a pore fluid pressure factor to give an effective coefficient ( $\mu_{eff} = \mu(1-\lambda)$ ; Equations 7-8). We set  $\mu_{eff} = 0.36$  (e.g., considering near-hydrostatic conditions with  $\lambda = 0.4$  and  $\mu = 0.6$ ) and a cohesion of 20 MPa (Table 1). At the trailing edges of the upper and subducting plates we add a weak region to mechanically isolate the subducting and overriding plates from the adjacent thermal

boundary layers that develop as the model evolves. These two weak regions are 30 km wide by 150 km deep with a constant yield stress of 1 MPa.

### 2.3.2 Crustal Rheology

For oceanic compositions, we use lookup tables (metabasalt, metagabbro) to impose the flow law associated with the weakest mineral predicted to be stable and hence dominate creep at those *P-T* conditions (Figure S1). In metamafic lithologies, dislocation creep flow laws are used for quartz (Hirth et al., 2001; as a stand-in for the blueschist facies glaucophane), amphibolite (Hacker & Christie, 1990), and eclogite (Zhang & Green, 2007). We adopt a dislocation creep quartz flow law for the pelagic sediment (Hirth et al., 2001). A maximum decoupling depth (MDD) of 200 km is chosen. That is, at depths greater than the MDD, the downgoing crust is assigned properties identical to the background mantle.

In terms of the plastic yield stress, we set the friction angle so that a  $\mu_{eff}$  of 0.36 is also used for metagabbro and upper plate crust (i.e., an equivalent yielding profile to that of the background mantle). We prescribe a lower yield stress within the 145 km long initially curved portion of the interface ( $\mu_{eff}$  = 0.005) to facilitate subduction initiation. A cohesion  $C_0$  of 1 MPa is used for pelagic sediment and metabasalt and 20 MPa for metagabbro (Table 1; Equation 7).

## 2.3.3 Serpentinite Rheology

Modeled serpentinite deforms via the Peierls creep mechanism (low-temperature plasticity; Burdette & Hirth, 2022). Peierls creep is implemented as a dislocation creep approximation of the Peierls creep flow-law (Kocks et al., 1975; Frost and Ashby, 1982):

11. 
$$\dot{\epsilon} = A\sigma^2 \exp\left(\frac{-Ea}{RT}\left(1 - \left(\frac{\sigma}{\tau_0}\right)^p\right)^q\right)$$

Where  $\tau_0$  is the low-temperature plasticity Peierls stress and p and q are empirical parameters, and Ea the activation energy for the Peierls mechanism. Unlike dislocation and diffusion creep (Equation 5), the Peierls creep flow law cannot be rearranged for stress because of the stress dependence in the exponent. Therefore, we use a dislocation creep-based approximation of low-temperature plasticity/Peierls creep (see Kameyama et al., 1999; Fildes & Billen, 2025; Text S1 for more details) with constants from Burdette & Hirth's

(2022) antigorite experiments. At each timestep, the stability field of serpentinite is checked based on a lookup table, and, if the composition is within serpentinite stability, the full Peierls creep flow law is used for model cells with above 10 wt. % serpentinite (Escartin et al., 2001), and therefore. In regions below 10 wt. % serpentinite, the serpentinite rheology is geometrically averaged along with the other composition(s) in the cell. Viscosity is thus reduced in regions where serpentinite exceeds the threshold. Outside of serpentinite stability we adopt the olivine rheology imposed on the background mantle. Water that would be re-released by deserpentinizing material is not tracked.

We also include a plastic yielding component in the serpentinite rheology. Reported serpentinite yield stresses span a broad range of values, depending on serpentine species, temperature, velocity, and pressure. For example, reported friction coefficients ( $\mu$ ) of lizardite range from 0.18 (Carpenter et al., 2009; Tesei et al., 2018) to  $\sim$  0.55 (Dengo & Logan, 1981; Moore et al., 1997), with many experiments falling in the 0.25-0.4 range (Moore & Lockner, 2004; Behnsen & Faulkner, 2012; Scuderi & Carpenter, 2022). Conversely, antigorite (the high temperature polymorph of serpentinite), generally has a higher coefficient of friction of 0.5-0.85 (Raleigh & Paterson, 1965; Reinen et al., 1994), which may be decreased if dissolution-precipitation creep enhances susceptibility to failure (Rutter, 1976; Behr & Platt, 2013; Tulley et al., 2024). Given this uncertainty, we explore a range of values for the serpentinite yield strength, with  $\mu_{\rm eff}$  = 0.01-0.04 and a cohesion of 1 MPa (i.e., considering  $\lambda \sim$  0.90-0.95 and  $\mu$  = 0.2-0.6; Table 1). We provide more detailed discussion and references on both the Peierls creep formulation and serpentinite yielding in the Supporting Information (Text S1).

3 Results

We first present our reference subduction model that includes serpentinite ingrowth over time. Next, we analyze similar models with variable  $H_2O$  inputs into the subduction zone, including with and without a sediment layer. Finally, we vary serpentinite strength to test the sensitivity of subduction kinematics and slab pressure-temperature (P-T) conditions to our rheological assumptions about the weak, accumulating serpentinite along the plate interface.

To ensure consistency in comparing serpentinite ingrowth across simulations, we compare model snapshots at timesteps with equivalent total amounts of subducted plate length (i.e., *net convergence*) and therefore equivalent amounts of net bound  $H_2O$  input from the portion of the downgoing slab beneath the variably hydrated sediment layer. We focus on timesteps at which the net convergence corresponds to approximately that required for the downgoing plate to reach the lower mantle (i.e., net convergence  $\sim 860$  km). For completeness, we also present comparisons at equivalent model times in the Supporting Information (Figure S3) as well as additional tests that individually exclude various complexities from the reference models, namely serpentinite, fluid-induced mantle weakening, and the use of phase diagram lookups to derive the density and viscosities of the interface/crustal lithologies (Figures S4-S7).

#### 3.1 Reference model

Because the models are dynamic, plate motions are not imposed and hence subduction geometries and velocities evolve freely through time, thereby impacting, and being impacted by, serpentinite ingrowth for 50 Myr (Figure 3). The co-evolving convergence rates, serpentinite content, and slab *P-T* profiles are displayed in Figure 4 for the reference model. The *P-T* profiles are overlain on the pseudosections used for pelagic sediment and metabasalt (Figure 4b-c), the two most hydrated lithologies of our model slab.

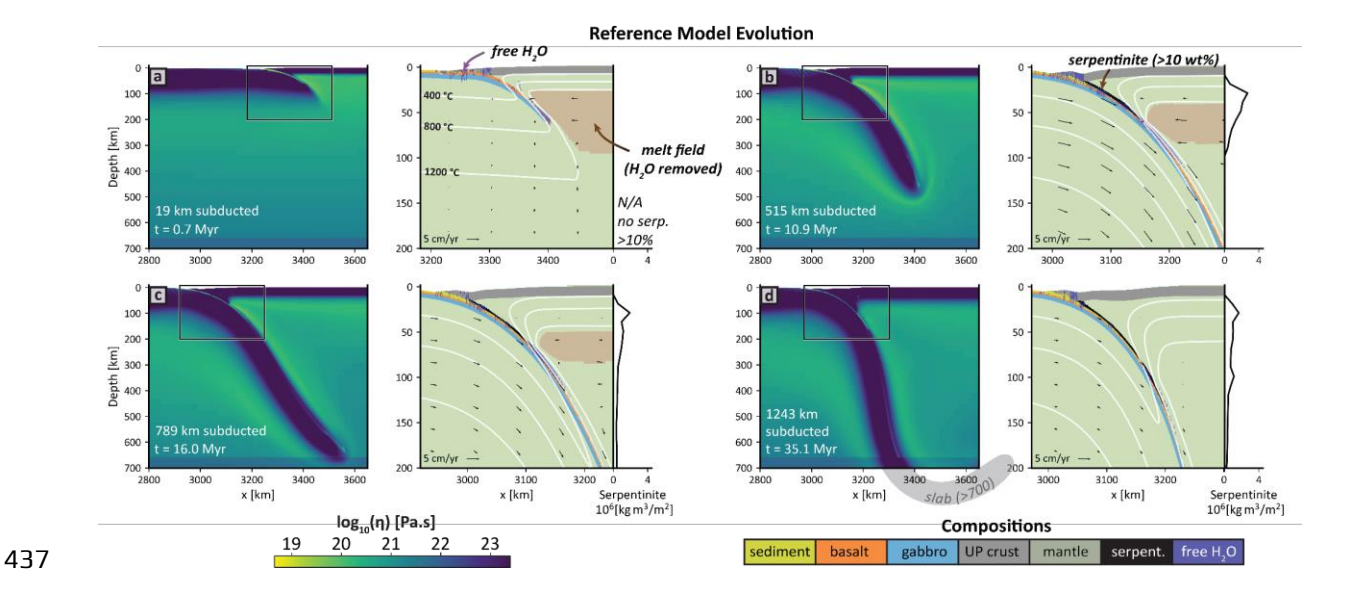


**Figure 3.** Snapshots of reference model evolution. (**a**, **b**) Model stages showing the initiation (Phase I) and free-sinking phases (Phase II), respectively, with the downgoing slab releasing free H<sub>2</sub>O that hydrates the mantle wedge via serpentinization ("cumulative serpentinization" shown). (**c**, **d**) Evolution just before (Phase II) and after (Phase III) the core of the slab passes the 660 km deep transition zone. (**d**) Grey shows extent of slab outside zoom-in region. To limit excess hydration of the overriding plate, a hydrous "melt" region is calculated (Katz et al., 2003), where free H<sub>2</sub>O is assumed to be incorporated into melt and removed from the system (see Methods, Section 2.2, for details).

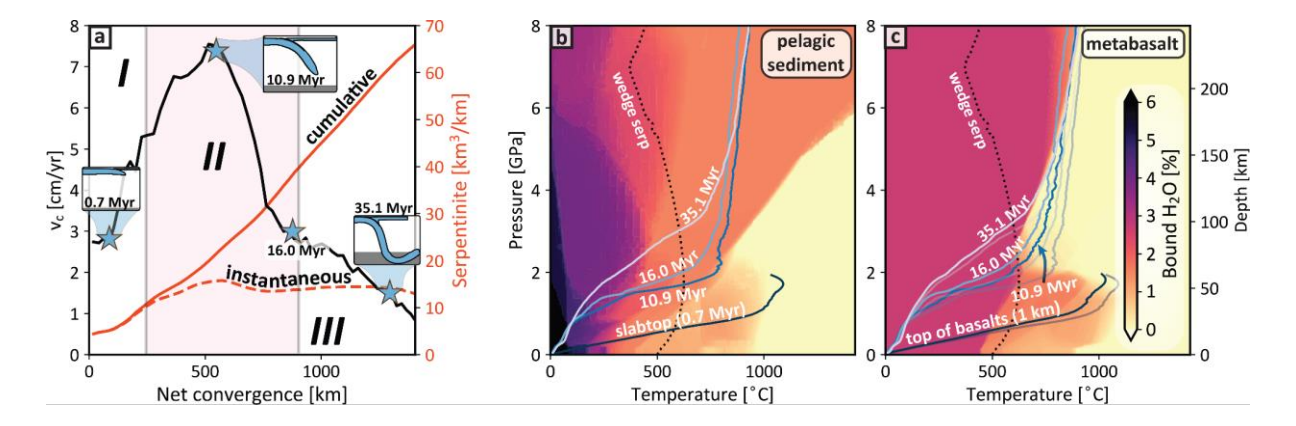


**Figure 4.** Kinematic and thermal evolution of the reference model. (a) Ingrowth of *cumulative* serpentinite produced over the course of the model, and *instantaneous* serpentinite content including serpentinite stable at a given point in time, i.e. without deserpentinized/downdragged material. *I* refers to the infancy stage, *II* to the free sinking phase, *III* to the mature phase as classified by previous studies (e.g., Holt & Condit, 2021). (b) Evolution of slabtop and (c) near slabtop thermal states. Background shows bound water used in lookups for pelagic sediments and metabasalts, respectively. Serpentine stability in the mantle wedge is also shown for reference. Lightly shaded *P-T* paths (c) coincide with the slabtop *P-T*, and darker shading coincides with *P-T* conditions at the top of the metabasalt section, 1 km deep normal to the plate interface.

During the subduction infancy stage (I), until  $\sim$  8 Myr, the slab largely sinks nearvertically (Figure 3a). Subduction is relatively sluggish but accelerates from  $\sim$  3 to 5.5 cm/yr (Figure 4a). Convergence is dominantly accommodated via rollback, with overriding plate motion initially ~ 5× faster than that of the subducting plate. This infancy stage is the hottest phase, with a slabtop significantly warmer than during the latter stages (Figure 4b). As a result, H<sub>2</sub>O is released from the downgoing oceanic crust into the mantle wedge only down to a maximum depth of  $\sim$  60 km at 0.7 Myr (Figure 3a). Released H<sub>2</sub>O migrates upwards until it either: 1) enters a region where melt is stable, where it is removed, or, 2) enters a region where serpentinite is stable, where it is bound in serpentinite in the mantle wedge (Figure 3c). During this initiation phase, serpentinite formed and dragged down over the total model run—cumulative serpentinite—is approximately equal to the instantaneous serpentinite—the amount of stable serpentinite in the mantle wedge at any given point in time. That is, there is minimal downdragging of serpentinite during the initiation stage. Additionally, there is relatively modest serpentinite production: Only <20% of cumulative serpentinization of the entire model duration is produced by the end of this phase (Figure 4a). At the beginning of this stage (0.7 Myr), the amount of serpentinite has not yet exceeded the 10 wt. % serpentinite per cell threshold that triggers the full weak serpentinite rheology (Figure 3a), and therefore the accelerating convergence rate is not due to serpentinite ingrowth, creating a layer 5 km thick (Figure S8).

During the following *free sinking phase (II)*, the tip of the downgoing plate approaches the 660 km transition at a steep dip (Figure 3b) before flattening out to a subhorizontal angle (Figure 3c). At this point, the convergence rate reaches its maximum value (Figure 4a), and both these higher advection rates of the sinking slab and thickening of the cold forearc region (i.e., an increase in the "decoupling depth") cause temperatures to cool by  $\sim 200~^{\circ}$ C at 3 GPa from 10.9 to 16.0 Myr. Such cooling has been seen in previous timedependent subduction models (Wang et al., 1995; Kincaid & Sacks, 1997; Holt & Condit, 2021; Turino & Holt, 2024). As a result of cooler temperatures, water release from the oceanic crust occurs at greater depths than during subduction infancy, down to 80 km (Figure 4c). However, water release in pelagic sediments has a shallow pulse at  $\sim 30~\text{km}$  that coincides with the depths of dehydration from the loss of stilpnomelane (Figure S9). Mantle

wedge serpentinite content is greatest shallower than 50 km (1.7 GPa) depth, approximately where these pelagic sediments dehydrate, while deeper dehydration arises from the dehydrating oceanic section (Figure 4b-c). Water released by slab dehydration causes more serpentinite to accumulate in the mantle wedge, increasing *instantaneous* serpentinite content by  $\sim 40\%$  over phase II from  $\sim 12 \text{ km}^3/\text{km}$  to a peak of  $\sim 16 \text{ km}^3/\text{km}$ . During this phase, serpentinite also begins to be dragged downwards to *P-T* conditions where serpentine is unstable and thus breaks down; hence, *instantaneous* serpentinite (stable in the interface/forearc) becomes significantly less than *cumulative* serpentinite. Therefore, during this stage, downdragging begins to exceed serpentinite ingrowth, causing the amount of instantaneous serpentinite in the mantle wedge to start to decrease (Figure 4a). However, throughout this phase, and in contrast to the earlier phase, enough serpentinite has accumulated to exceed the 10 wt. % serpentinite lubrication threshold along the interface, and therefore the plate interface is lubricated by serpentinite (Figure 3b-c).

The sinking of the slab into the lower mantle, past the 660 km transition zone, marks the beginning of the *mature phase* (III; Figure 3d). After  $\sim 17.6$  Myr (the boundary between phase II and III), convergence rates decrease to below 2 cm/yr; this slowdown is driven by the slab penetrating the high viscosity lower mantle. Slab *P-T* conditions are too cold for metabasalts and metagabbros to dehydrate within the serpentinite field, and any additional dehydration must come from metasediments (Figure 4b). Dehydration of metasediments continues, causing the *cumulative* serpentinite to progressively increase. However, most newly formed serpentinite is dragged downwards (Figure 3d). In fact, downdragging slightly outpaces ingrowth, causing instantaneous serpentinite to decrease  $\sim 5\%$  from 17.6 to 50 Myr (Figure 4a).

### 3.2 Variable H<sub>2</sub>O input

To examine the effect of mineral-bound  $H_2O$  content on slab dehydration and forearc serpentinization, we vary water content in the downgoing 1 km-thick sediment layer, comparing a "fully saturated" case with the maximum amount of mineral-bound  $H_2O$  (6.89 wt. %), our intermediate, moderately hydrated reference case (4 wt. %  $H_2O$ ), and a completely anhydrous case with 0%  $H_2O$  (Figure 5a-c). Additionally, we include a limiting case identical to those shown in Figure 5a-c but with no sediment layer above the

metabasalts (Figure 5d). In both the anhydrous and no-sediment cases, H<sub>2</sub>O is released exclusively from the metabasalts and metagabbros.

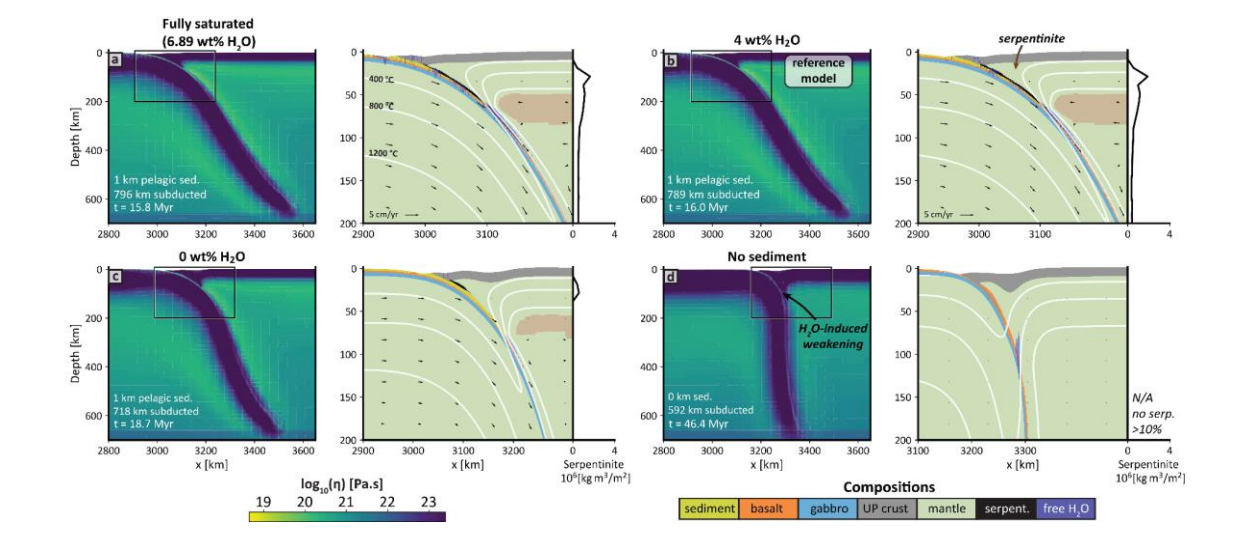


**Figure 5.** Snapshots of models while varying the hydration state of the incoming sediment. To standardize the amount of bound water input into the subduction zone, all model time slices are shown for the same distance subducted, approximately enough to reach the 660 km transition zone. (**a-c**) Models showing variation in sediment hydration state from fully hydrated to anhydrous (6.89% to 0%). (**d**) No sediment but with other lithologies (metabasalt, metagabbro) still initially hydrated.

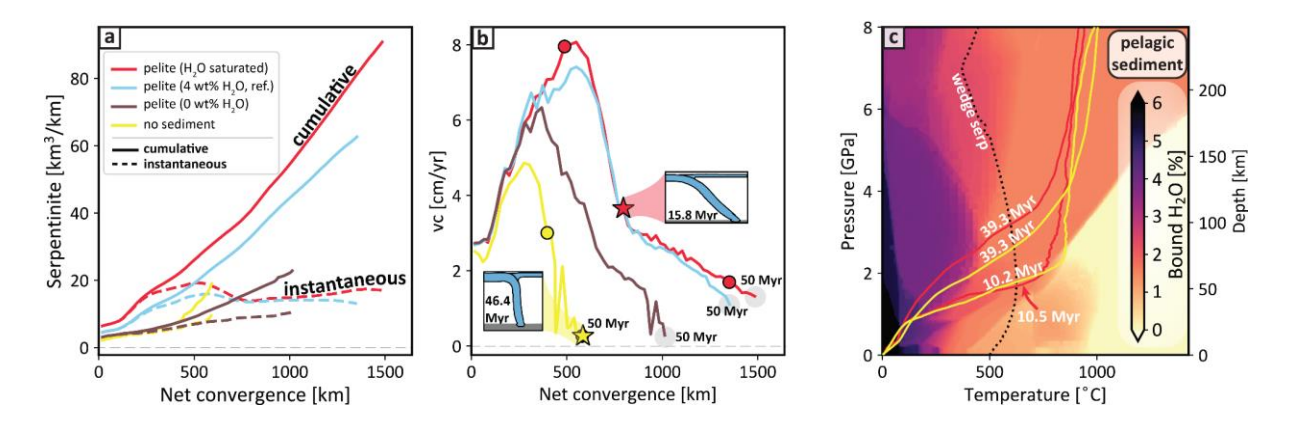


**Figure 6.** Kinematic and thermal evolution of models with varying water content in sediment or without sediment. (**a**) Ingrowth of serpentinite over the course of the model run either considering the cumulative serpentinite that includes both stable serpentinite and deserpentinized material or the instantaneous amount that only includes the amount of serpentinite that is stable. (**b**) Plate convergence rates for different models. Filled circles denote times when slabtop *P-T* conditions are plotted in **c**. (**c**) Slab *P-T* profiles at two model timesteps for the fully saturated and no sediment cases overlain on the pseudosection for pelagic sediment.

Incoming plates with different amounts of incoming bound water subsequently release variable amounts of water that migrate into the mantle wedge to produce serpentinite. The greatest amounts of serpentinite are produced in the fully saturated case, both for total *cumulative* serpentinite, which includes deserpentinized material, and *instantaneous* serpentinite. In the fully saturated case, there is therefore the most serpentinite available to lubricate the interface (Figure 5a). The fully saturated and moderately hydrated cases both produce more serpentinite than the anhydrous case and the case without a sediment layer. The fully saturated and moderately saturated cases also reach a quasi-steady state, but the anhydrous (0 wt. %) case and case without sediment do not (Figure 6a).

In the case without a sediment layer, there is no sediment to insulate the metabasalt layer at the interface, and so the hydrated metabasalts are directly exposed to the hotter temperatures in the mantle wedge (Figure S10). As a result, the metabasalts are hotter, dehydrate more completely, and more cumulative serpentinite is produced in this model than within the anhydrous case. This case without a sediment layer, however, drags down more serpentinite, which acts to reduce the volume of stable *instantaneous* serpentinite in the wedge to levels comparable to the case with a layer of sediment. There is more downdragging because the rheology of metabasalts of the oceanic crust follows a strong, eclogite flow law above  $\sim 1.5$  GPa (i.e.  $\eta_{eclogite} >> \eta_{antigorite}$ ), whereas the rheology of sediments is governed by a weaker, quartz flow law.

As seen in previous numerical subduction models (e.g., Čížková & Bina, 2013; Behr et al., 2022), a weaker plate interface results in faster convergence rates. However, in this suite of models, variations in effective plate interface strength result from varying volumes of weak serpentinite. During subduction infancy, serpentinite begins to accumulate but not in sufficient volumes to yet exert a lubricating effect: the convergence rates in all models evolve similarly and are accelerating, although the case without sediment is  $\sim 0.5 \, \text{cm/yr}$  slower at the start of the model because there is no sediment to weaken the interface (Figure 6b). After the initiation stage, the case with the most incoming water has the highest degree of serpentinite production and experiences the fastest convergence rates ( $\sim 8 \, \text{cm/yr}$ ), whereas the anhydrous case reaches maximum convergence rates of  $\sim 6 \, \text{cm/yr}$ . Cases with no pelagic sediment only reach a maximum convergence rate of  $\sim 5 \, \text{cm/yr}$  and

become locked by the end of the model run (Figure 6b). This locking coincides with an increase of the interface viscosity by approximately two orders of magnitude (Figure S8) because serpentinite accumulation that could weaken the interface is relatively low (Figure 5). The variation in slab dip is also linked to differences in the amount of water release and serpentinite formed (Figures 5, 6a). As the slab without sediment reaches the highly viscous 660 km transition zone, and convergence rates slow to <1 cm/yr, the dip increases dramatically. Therefore, the ingrowth of weak serpentinite produces slabs with higher convergence rates and shallower dips, whereas the case with no water has more downdragging of serpentinite, lower convergence rates, and higher dips.

Thermal state is, in turn, linked to subduction kinematics. The models with faster convergence rates, due to greater serpentinite volumes and therefore a weaker interface, have a cooler slabtop due to more rapid downward advection of cold lithospheric plate. In contrast, the case without sediment and with slow convergence has a warmer slabtop (Figure 6c) due to feedbacks between serpentinization, interface strength, and convergence rate.

# 3.3 Variable Yield Strength

Finally, we test the effect of serpentinite yield strength on model evolution, with snapshots of the slab morphology for models with serpentinite strength again plotted for equivalent net plate convergence (Figure 7). We vary yield strength values by adjusting the effective coefficient of friction  $\mu_{eff}$  from 0.01 to 0.04, above and below the reference value of 0.02 (Equation 7).

The *cumulative* amount of serpentinite created over the whole model duration is approximately equivalent for any amount of convergence regardless of serpentinite strength (Figure 8a). However, different serpentinite strengths lead to different degrees of downdragging that impact both the instantaneous serpentinite amounts and hence convergence rates over time. During the initiation stage (slab depths < 400 km), all models evolve similarly, with little variation in the downdragging of serpentinite (Figure 8a-b). However, after the initiation stage, serpentinite retention is very sensitive to serpentinite strength: weak forearc serpentinites with low friction coefficients are dragged down more easily than those with high friction coefficients, despite similar cumulative serpentinite

ingrowth. That is, the serpentinite stable at any given time—the *instantaneous* serpentinite—is affected by downdragging. At the end of the free sinking phase there is  $\sim$  40% more instantaneous serpentinite in the high friction case ( $\mu_{eff}$  = 0.04) compared to the case with the weakest yielding parameters ( $\mu_{eff}$  = 0.01; Figure 7). An even higher friction coefficient of 0.06 was separately tested and, in line with this trend, resulted in the most serpentinite retention and the least downdragging (Figure S11).

These differences in serpentinite strength, and hence retention and downdragging, are linked to changes in kinematics and thermal state. The case with the lowest serpentinite strength reaches maximum convergence rates of nearly 9.4 cm/yr, whereas the strongest case plotted has maximum convergence rates that are lower by 30% (Figure 8b). Therefore, even though there is more instantaneous serpentinite in the wedge in the high strength case, it is the high strength of serpentine, not the abundance, that exerts a larger influence on kinematics and produces the lower convergence rates. Finally, the lower convergence rates in the higher strength case produce warmer slab *P-T* conditions (Figure 8c) because the slab experiences more diffusive heating from the overlying mantle wedge. This difference in temperature does not lead to a significant difference in cumulative serpentinite production because the slab *P-T* conditions still pass through the same dehydration reactions (Figure 8c).

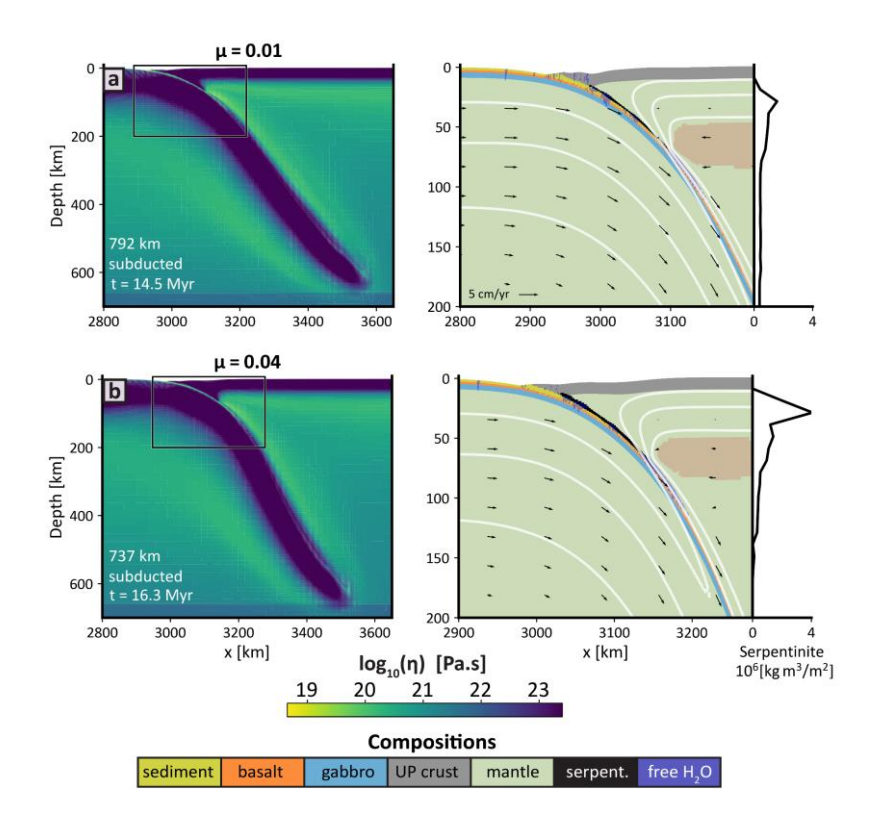


**Figure 7.** Snapshots of the subducting plate as a function of friction parameters in serpentinite with all other parameters identical to the reference model, shown in Figure 3. All cases are plotted at the same timestep, approximately the time for the subducting plate to reach the transition zone.

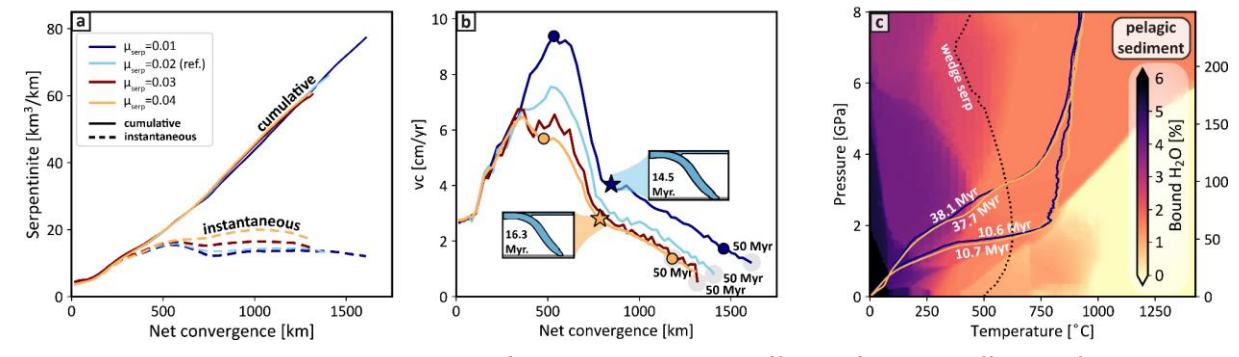


**Figure 8.** Kinematic and thermal evolution of models with variable effective friction coefficient of serpentinite. (a) Ingrowth of serpentinite over the course of the model run either considering the *cumulative* serpentinite amount that was created over the duration of the entire model run or the *instantaneous* amount that indicates the amount of serpentinite that is stable at any given point in time. The difference between the two is an indication of the degree of loss of serpentinite due to coupling with the downgoing plate. (b) Changes in convergence rate for different models as a function of serpentinite strength. Filled circles denote times when slabtop *P-T* conditions are plotted in **c**. (c) The thermal state at two snapshots in time for the strongest and weakest plotted endmembers of serpentinite strength.

#### 4 Discussion

628

629

630

631

632

633

634

635

636

637

638

639

640

641

642

643

644

645

646

647

648

649

650

651

652

653

654

655

656

657

# 4.1 Ingrowth of serpentinite

Despite exerting a critical influence on magmatism, seismicity, and the exhumation of rocks from depth, the mantle wedge remains one of the most enigmatic regions of the subduction system. In particular, the amount of water bound in hydrous minerals, particularly serpentinite, is poorly resolved, partly due to the paucity of phase changes in wedge serpentinites, which complicates efforts to precisely constrain pressure-temperature (P-T) conditions that those rocks experienced. Unlike many crustal rocks, serpentinites rarely contain minerals suitable for geochronology. Consequently, constraining the ingrowth of serpentinites in the mantle wedge, as well as linking them to large-scale subduction evolution, necessitates alternative approaches, such as geochemical analyses of arc magmas or serpentinite mud volcanoes, geophysical techniques, and numerical modeling (e.g., Tatsumi, 1986; Tatsumi & Eggins, 1995; Fryer et al., 1999; Hyndman & Peacock, 2003; Abers et al., 2017). Linking mineral phase stability calculations in the downgoing plate to thermomechanical models provides a quantitative framework for evaluating serpentinite stability and the amount of water released by the slab. Our numerical models expand on this framework by integrating the thermal state of the downgoing slab to its dewatering processes, the resulting mantle wedge hydration over time, and subsequent rheological transformations, thereby complementing petrological and geochemical techniques (e.g., Scambelluri & Tonarini, 2012).

This work examines the effects of the progressive ingrowth and buildup of serpentinite in the mantle wedge over the lifetime of a subduction zone (Figures 4-8) within dynamic models that implicitly contain feedbacks between thermal structure, dehydration, serpentinite accumulation, and resultant interface strength changes. Extensive geodynamic and petrological modeling has shown that water released from the downgoing slab hydrates and serpentinizes the forearc mantle wedge (e.g., Peacock, 1987; Wada & Wang, 2009; Abers et al., 2017; Condit et al., 2020). These studies have successfully tracked serpentinization in the context of exhumation, wedge dynamics, magmatism, and/or decoupling of the downgoing slab from the overriding wedge (Gerya et al., 2002; Arcay et al., 2005; Nikolaeva et al., 2008; Gerya & Meilick, 2011; Li et al., 2019; Kerswell et al., 2021).

Previous work has already examined some feedbacks caused by serpentinization. For instance, rapid serpentinization during subduction infancy has been linked to evolving temperatures in the slab (Epstein et al., 2024), and interface strength has been shown to modulate both force balances (Lamb & Davis, 2003; Arcay et al., 2005; Gerya et al., 2008) and plate convergence rates (Conrad & Hager, 1999; Behr & Becker, 2018; Behr et al., 2022). However, how the time-dependent ingrowth of serpentinites, and thus the development of a weak interface, feed back into subduction kinematics, such as plate velocities and slab morphology, was beyond the scope of most previous studies. A select few studies, however, use dynamic numerical models to explore the impact of mantle hydration-induced weakening on subduction, but with a weakening and density parameterization not specific to serpentinization (Nakao et al. 2016, 2018; Ritter et al., 2024). These studies revealed feedbacks between large-scale kinematics and hydration-induced weakening of the mantle wedge, a result confirmed by our work, as well as convergence rate slowdowns associated with buoyancy from abyssal hydration of the downgoing plate. Apart from the above, such feedbacks are rarely incorporated in detail into dynamic and time-dependent subduction modeling studies. Instead, many studies typically impose kinematic boundary conditions usually plate velocities—and hence prevent the progressively accumulating weak serpentinite from influencing large-scale plate motions. In contrast, our dynamic models allow plates to evolve freely, capturing key feedbacks between serpentinite rheology, mantle wedge hydration, and thermal state.

658

659

660

661

662

663

664

665

666

667

668

669

670

671

672

673

674

675

676

677

678

679

680

681

682

683

684

685

686

687

688

The extent of serpentinization of the mantle wedge over time is a mass balance between serpentinite ingrowth and loss. Ingrowth of mantle wedge serpentinite depends on the amount of water released from the downgoing slab, depending on the thermal state. From the exhumed rock record, slabs are predicted to be warmest during the earliest phases of subduction, after which they cool down (Platt, 1975; Cloos, 1985; Agard et al., 2018; Penniston-Dorland et al., 2025). In dynamic subduction models, such as presented herein, this thermal evolution emerges as both slab sinking accelerates and the base of the cold forearc (i.e., the "decoupling depth") migrates to greater depths above the slab (Figures 3-4; cf. Holt & Condit, 2021). Recent work shows that this time-evolving thermal structure exerts a significant impact on predictions of slab dehydration and mantle forearc serpentinization (Epstein et al., 2024). Our work finds similar results: initial rates of

serpentinization are fastest during the hot, early stages, when the slab can fully dehydrate, and before significant volumes of serpentinite have begun to be dragged down into the deeper mantle.

Serpentinite ingrowth is also strongly influenced by the composition of the downgoing material that uniquely responds to the P-T conditions it encounters. Hydrated sediment produces more water that drives serpentinization in the mantle wedge compared to metagabbros and metabasalts (Figure 5). More serpentinization in sediment-rich models was originally shown for a sediment with an averaged sediment composition (GLOSS), which also tends to dehydrate at shallower conditions than metabasalts (Rüpke et al., 2004). Greater serpentinization extents with more sediment are also consistent with more recent modeling (Abers et al., 2017; Epstein et al., 2024). Models without sediment result in less mantle wedge serpentinization because the package of subducting metabasalts on average contain less water than pelagic sediment (2.3 wt.% vs. 6.89 wt.%) and dehydrate at P-T conditions outside those of serpentine stability, particularly as the model matures (Figures 5-6). Although other siliciclastic sediment compositions may exhibit different dehydration patterns, a global assessment of the most common subducting sediment compositions (Plank & Langmuir, 1998) finds pelagic sediments to be the most prevalent. Non-siliciclastic compositions, such as carbonate-rich sediments, undergo devolatilization to produce complex, mixed-volatile fluids, which may further weaken the plate interface (Oyanagi & Okamoto, 2024), but decarbonation and consideration of high-solute fluids is beyond the scope of the current work.

Downdragging represents an additional complexity by removing previously accumulated serpentinite from the mantle wedge. Significant coupling between serpentinite and the downgoing slab was originally proposed as a mechanism to delay dehydration of material in or near the slab until it reaches depths necessary for generating hydrous arc magmas (Tatsumi, 1986). This is also evidenced geochemically by the striking similarity between forearc serpentinites and arc magmas (Tonarini et al., 2011; Scambelluri et al., 2019). From a mass balance perspective, downdragging would prevent some forearcs from being oversaturated (Savov et al., 2007; Abers et al., 2017; Epstein et al., 2024). However, the balance between coupling and downdragging has largely been modeled in the context of subduction erosion (Angiboust et al., 2012), the formation of a subduction channel

(Schwartz et al., 2001; Gerya et al., 2002; Hilairet & Reynard, 2009; Gerya & Meilick, 2011), and downdragging of water bound in the mantle (Nakao et al., 2016, 2018). While we only consider a limited range of serpentinite strengths in our time-dependent models (Figure 7), our results agree with more extensive targeted modeling demonstrating that serpentinite downdragging depends on serpentinite rheology (Douglas et al., 2023). We find that cases with low effective friction coefficients (0.01) have ~ 2× more *cumulative* serpentinite than is currently stable as *instantaneous* serpentinite, while the high friction case (0.04) has only ~ 35% more *cumulative* serpentinite (values extracted at the timesteps with maximum convergence rates). Nonetheless, a rheologically weak layer of serpentinite ~ 5 kilometers thick above the downgoing slab forms and stabilizes within our models with sediment, which is broadly consistent with, for example, recent seismological estimates using receiver functions in Cascadia (Figure S8; Audet et al., 2025).

# 4.2 Effects of serpentinite ingrowth on plate kinematics

The potential link between slab fluid release, interface strength, and hence subducting plate deformation was first recognized during the plate tectonics revolution. Studies noted that mineralogically-bound volatiles would be liberated during subduction and weaken the plate interface (Isacks et al., 1968; Isacks & Molnar, 1971). A weakening of the interface affects the stress state along the interface and thus the overall subduction zone force balance over both long and short timescales (e.g., King & Hager, 1990; Conrad & Hager, 1999; Behr & Becker, 2018; Julve et al., 2024).

#### **Subduction Infancy**

#### Free sinking & mature phases

# sediment-starved endmember slower convergence hot 700 °C slab hydrated sediment-rich endmember faster convergence not 700 °C slab hot 70

**Figure 9.** Summary of evolutionary feedback in our numerical results. The ingrowth of serpentinite reduces shear stress along the plate interface, changing plate convergence rates, which in turn can change the thermal state over time. All three processes are interconnected and can accentuate the influence of weak, hydrated subducting lithologies, such as sediment, on plate speeds. Shaded regions in the free sinking/mature phase correspond to regions of active serpentinization.

An array of processes may lubricate the plate interface, thereby reducing interface shear resistance, and, in turn, elevating plate speeds. In particular, the interface may be lubricated by sediment or ingrowing serpentinite. However, unlike sediment (Lamb, 2006; Pusok et al., 2021; Behr et al., 2022) or mantle wedge hydration (Arcay et al., 2005; Wada & Wang, 2009; Gerya & Meilick, 2011; Nakao et al., 2016, 2018; Ritter et al., 2024), the direct impact of interface/wedge serpentinization on plate evolution has rarely been explicitly examined in fully dynamic models. In our models, serpentinite accumulation elevates convergence rates after subduction infancy as, during the earliest phase, weak serpentinite has not yet accumulated to sufficient degrees to significantly reduce the interface stress state. However, during the following free-sinking phase, greater volumes of weak serpentinite have accumulated, causing reduced shear stresses along the interface and thus faster convergence rates (Figure 5). Therefore, in our models, sediments weaken the interface by both reducing the in-situ strength of the interface, as previously shown, and by

releasing water and weakening the interface further via the progressive formation of weak serpentinite. Instantaneous serpentinite increases by 20-40 % during the mature and free sinking phases, compared to subduction infancy, and so the associated convergence rate increase is similarly time dependent (Figure 9).

A weaker interface has also been linked to the formation of a subduction channel (Shreve & Cloos, 1986) which, when dominated by buoyant serpentinite, may aid the exhumation of negatively buoyant lithologies, such as eclogites, from mantle depths (e.g., Schwartz et al., 2001; Gerya et al., 2002). Because we find time-dependent ingrowth of serpentinite, we expect that the ability for a serpentinite or serpentinite-dominated subduction channel to entrain and exhume other lithologies may also be time-dependent. As subduction matures, the progressive ingrowth of serpentinite weakens the interface more, meaning that return flow in a serpentinized subduction channel might be a more viable mechanism of exhumation after subduction reaches maturity and when the slabtop temperatures are generally lower than earlier stages. However, we do not observe large-scale exhumation in our models: additional mechanisms such as extensive surface erosion, greater channel buoyancy, or plate velocity changes (cf. England & Richardson, 1977; Ring et al., 1999; England & Smye, 2023) are likely needed.

Serpentinite is expected to be common along the plate interface, and therefore we expect that interface weakening is also tied to water release from hydrated lithologies, such as sediments, instead of inherently weak lithologies alone. A specific comparison to plate speeds is challenging because of other factors that affect subduction that include plate age, plate and trench geometry, overriding plate deformation, and forces associated with mantle flow (e.g., Isacks et al., 1968; Lallemand et al., 2005; Ueda et al., 2008; Jagoutz et al., 2015).

# 4.3 Model limitations and assumptions

Because we target the first-order impacts of serpentinization on subduction dynamics, and vice versa, some model simplification is necessary. The first set of assumptions pertains to initial conditions, model geometry, and numerical limitations. For example, model resolution modestly impacts the absolute quantities of serpentinite generated in the wedge. The current maximum model resolution is  $\sim$  1.3 km; increasing model resolution to 0.7 km increases instantaneous serpentinization by up to 15%, but the

first-order trends are unchanged (Figure S12). Additionally, we impose a maximum decoupling depth of 200 km by stiffening the crust (to the viscosity of the background mantle) at this depth. While this does not impact subduction zone thermal structure during the earlier subduction phases—during which the lower limit of the cold forearc much shallower—the incorporation of self-consistent, shallower decoupling depth would likely make the slabtop temperatures warmer (> 30 Myr; Figure 4) and hence more compatible with mantle melting, arc volcanism, and surface heat flow during the mature phase (e.g., Furukawa, 1993; Wada and Wang, 2009). Finally, shear heating, not considered here, would also increase the slabtop temperature (e.g., Gao & Wang, 2014; Peacock, 1992; Penniston-Dorland et al., 2015; England & Smye, 2023) and may increase dehydration and serpentinization extents (Hernández-Uribe & Palin, 2019).

Care must also be taken in interpreting our models and others that make similar simplifying assumptions about the treatment of fluid flow and serpentinization. Free water is assumed to migrate directly upwards relative to the surrounding matrix, as is common in subduction modeling studies (e.g., Magni et al., 2014; Menant et al., 2019). However, channelization in the wedge or slab interface is possible as suggested by stable isotope and trace element arguments from former interface units that have since been exhumed (e.g., Bebout & Penniston-Dorland, 2016; Epstein et al., 2021) and modeling studies with porous fluid flow (Wilson et al., 2014; Cerpa & Wada, 2025). This assumption may impact the absolute quantities of serpentinite that our models predict. For example, after 50 Myr, our models predict the ingrowth of  $\sim$  20% of instantaneous serpentinite of the Epstein et al. (2024) models, which assume perfect vertical transfer of fluids. Additionally, the hydration process we chose is designed to be conservative by requiring that 100% of a cell be serpentinized before any higher cells are affected, as suggested by the presence of H<sub>2</sub>O being the primary limiting factor to serpentinization (Peacock, 1987). Upward-migrating swarms of earthquakes—likely indicating channelized fluid migration—suggest that not all fluid is immediately bound through reaction with peridotite upon reaching the wedge, and partial serpentinization is possible (Davies, 1999; Halpaap et al., 2019).

We rely on a closed-system, equilibrium thermodynamic model to determine fluid release and flow laws during progressive subduction. Such models do not account for reaction overstepping, and are calculated in a closed system domain for all chemical

components other than H<sub>2</sub>O. Kinetic limitations to reactions shown by field studies, (e.g., in exhumed wedge serpentinite: Peacock, 1987; in eclogite: Putnis and Austrheim, 2010) are not taken into account, and may influence the thermal-rheologic feedbacks. The assumption of a closed system for non-volatile components means that the initial composition has a significant control on dehydration systematics. For example, we assume the downgoing sediments are pelagic. Non-siliciclastic compositions, such as carbonate-rich sediments, undergo devolatilization to produce complex, mixed-volatile fluids, which may further weaken the plate interface (Oyanagi & Okamoto, 2024). Lastly, and, perhaps most important, we cannot model melt transport or fluid-induced metasomatic (i.e., opensystem) reactions. Though weak hydrous minerals generated by metasomatism (Behnsen & Faulkner, 2012; Lindquist et al., 2023), such as talc and chlorite (Peacock & Wang, 2021; Codillo et al., 2022; Oyanagi and Okamoto, 2024; Easthouse et al., 2025; Klein & Behn, 2025) are potentially less abundant than serpentine, they are considerably weaker than serpentine and may therefore exert a significant effect on plate strength. Overall, interface strength, plate speeds, and slab temperatures will evolve as weak, hydrous lithologies accumulate along the interface (Figure 9).

## **5 Conclusions**

822

823

824

825

826

827

828

829

830

831

832

833

834

835

836

837

838

839

840

841

842

843

844

845

846

847

848

849

850

This study tracks serpentine buildup in the mantle wedge during subduction to reveal feedbacks between slab dehydration/forearc hydration, plate kinematics, dehydration, and slab thermal state over time. Feedbacks are included by allowing plate geometries and velocities to evolve freely within dynamic models, thereby capturing the highly time-dependent effects of serpentinization on large-scale subduction. Our models suggest:

- 1) As the downgoing plate dehydrates, the mantle wedge is progressively serpentinized over the lifetime of a subduction zone.
- 2) Serpentinite accumulation is modulated by the balance between wedge hydration and downdragging along the interface due to coupling with the downgoing plate.
- 3) Serpentinite ingrowth elevates subduction zone convergence rates because it weakens the plate interface. This is particularly pronounced during the intermediate-

- to-mature phases of subduction, after sufficient serpentinite has accumulated and reduced the interface strength.
  - 4) Exhumation of serpentinites may be favored after subduction infancy, i.e. once a sufficient quantity of serpentinite has accumulated in the mantle wedge.

Our work links two previously proposed hypotheses in subduction zone evolution: weakening of the interface due to the subduction of sediments and weakening of the interface due to the ingrowth of hydrous minerals. The lubricating effect of serpentinite likely acts in concert with that of subducted sediments, especially during the intermediate-to-mature phases of subduction.

# **Acknowledgments**

This work was supported by NSF grants EAR-2119842 to Holt, EAR-2119843 to Guevara, and EAR-2119844 to Condit. We thank Valeria Turino for helpful discussions and for providing a preprocessing script used in this study. We also thank the Computational Infrastructure for Geodynamics (geodynamics.org), which is funded by the National Science Foundation under award EAR-0949446 and EAR-1550901 for supporting the development of ASPECT. Computational resources were provided by NSF ACCESS under allocation EES-220058 to Holt.

#### **Conflict of Interest Statement**

The authors have no conflicts of interest to disclose.

# **Open Research**

The parameter files, visualization scripts, and code to run the numerical models in the study are available on Zenodo with the GPL-2 license via Stoner et al. (2025).

#### References

- Abers, G. A., Van Keken, P. E., & Hacker, B. R. (2017). The cold and relatively dry nature of mantle forearcs in subduction zones. *Nature Geoscience*, *10*(5), 333–337.
- Agard, P., Plunder, A., Angiboust, S., Bonnet, G., & Ruh, J. (2018). The subduction plate interface: rock record and mechanical coupling (from long to short timescales).

878	Lithos, 320–321, 537–566.
879	https://doi.org/https://doi.org/10.1016/j.lithos.2018.09.029
880	Amiguet, E., Van De Moortèle, B., Cordier, P., Hilairet, N., & Reynard, B. (2014). Deformation
881	mechanisms and rheology of serpentines in experiments and in nature. Journal of
882	Geophysical Research: Solid Earth, 119(6), 4640–4655.
883	https://doi.org/https://doi.org/10.1002/2013JB010791
884	Angiboust, S., Ioannidi, P. I., & Muldashev, I. (2024). Garnet fracturing reveals ancient
885	unstable slip events hosted in plate interface metasediments. Earth and Planetary
886	Science Letters, 640, 118794.
887	Angiboust, S., Wolf, S., Burov, E., Agard, P., & Yamato, P. (2012). Effect of fluid circulation on
888	subduction interface tectonic processes: Insights from thermo-mechanical numerical
889	modelling. Earth and Planetary Science Letters, 357, 238–248.
890	Arcay, D., MP. Doin, E. Tric, R. Bousquet, and C. de Capitani (2006), Overriding plate
891	thinning in subduction zones: Localized convection induced by slab dehydration,
892	Geochemistry Geophysics Geosystems, 7, Q02007, doi:10.1029/2005GC001061.
893	Arcay, D., Tric, E., & Doin, MP. (2005). Numerical simulations of subduction zones: Effect of
894	slab dehydration on the mantle wedge dynamics. Physics of the Earth and Planetary
895	Interiors, 149(1–2), 133–153.
896	Audet, P., & Bürgmann, R. (2014). Possible control of subduction zone slow-earthquake
897	periodicity by silica enrichment. <i>Nature</i> , <i>510</i> (7505), 389–392.
898	Audet, P., McLellan, M., & Bloch, W. (2025). Structure and serpentinization of the northern
899	Cascadia mantle wedge corner from receiver function modelling. Canadian Journal of
900	Earth Sciences, 62(4), 909-922.
901	Bangerth, Wolfgang, Juliane Dannberg, Menno Fraters, Rene Gassmöller, Anne Glerum,
902	Timo Heister, Robert Myhill, and John Naliboff. 2023. Geodynamics/Aspect: ASPECT
903	2.5.0 (version v2.5.0). Zenodo. <a href="https://doi.org/10.5281/ZENODO.8200213">https://doi.org/10.5281/ZENODO.8200213</a> .
904	Balázs, A., Faccenna, C., Gerya, T., Ueda, K., & Funiciello, F. (2022). The dynamics of forearc–
905	back-arc basin subsidence: Numerical models and observations from mediterranean
906	subduction zones. Tectonics, 41 (5), e2021TC007078.
907	Bebout, G. E., & Penniston-Dorland, S. C. (2016). Fluid and mass transfer at subduction
908	interfaces—The field metamorphic record. Lithos, 240–243, 228–258.
909	https://doi.org/10.1016/j.lithos.2015.10.007

910	Becker, T. W. (2006). On the effect of temperature and strain-rate dependent viscosity on
911	global mantle flow, net rotation, and plate-driving forces. Geophysical Journal
912	International, 167(2), 943–957.
913	Behnsen, J., & Faulkner, D. R. (2012). The effect of mineralogy and effective normal stress
914	on frictional strength of sheet silicates. Journal of Structural Geology, 42, 49–61.
915	Behr, W. M., & Becker, T. W. (2018). Sediment control on subduction plate speeds. <i>Earth</i>
916	and Planetary Science Letters, 502, 166–173.
917	Behr, W. M., & Bürgmann, R. (2021). What's down there? The structures, materials and
918	environment of deep-seated slow slip and tremor. Philosophical Transactions of the
919	Royal Society A, 379(2193), 20200218.
920	Behr, W. M., Holt, A. F., Becker, T. W., & Faccenna, C. (2022). The effects of plate interface
921	rheology on subduction kinematics and dynamics. Geophysical Journal International,
922	230(2), 796–812.
923	Behr, W. M., & Platt, J. P. (2013). Rheological evolution of a Mediterranean subduction
924	complex. Journal of Structural Geology, 54, 136–155.
925	Billen, M. I., & Arredondo, K. M. (2018). Decoupling of plate-asthenosphere motion caused
926	by non-linear viscosity during slab folding in the transition zone. Physics of the Earth
927	and Planetary Interiors, 281, 17–30.
928	Billen, M. I., & Hirth, G. (2005). Newtonian versus non-Newtonian upper mantle viscosity:
929	Implications for subduction initiation. Geophysical Research Letters, 32(19).
930	Boneh, Y., Pec, M., & Hirth, G. (2023). High-pressure mechanical properties of talc:
931	Implications for fault strength and slip processes. Journal of Geophysical Research:
932	Solid Earth, 128(3), e2022JB025815.
933	Burdette, E., & Hirth, G. (2022). Creep rheology of antigorite: Experiments at subduction
934	zone conditions. Journal of Geophysical Research: Solid Earth, 127(7),
935	e2022JB024260.
936	Carpenter, B. M., Marone, C., & Saffer, D. M. (2009). Frictional behavior of materials in the
937	3D SAFOD volume. <i>Geophysical Research Letters</i> , 36(5).
938	https://doi.org/https://doi.org/10.1029/2008GL036660
939	Cerpa, N. G., & Wada, I. (2025). Hydration state and updip fluid migration in the slab
940	mantle. Journal of Geophysical Research: Solid Earth, 130(6), e2024JB030609.

941	Chernak, L. J., & Hirth, G. (2010). Deformation of antigorite serpentinite at high temperature
942	and pressure. Earth and Planetary Science Letters, 296(1–2), 23–33.
943	Čížková, H., & Bina, C. R. (2013). Effects of mantle and subduction-interface rheologies on
944	slab stagnation and trench rollback. Earth and Planetary Science Letters, 379, 95-
945	103. https://doi.org/10.1016/j.epsl.2013.08.011
946	Cloos, M. (1985). Thermal evolution of convergent plate margins: Thermal modeling and
947	reevaluation of isotopic Ar-ages for blueschists in the Franciscan Complex of
948	California. Tectonics, 4(5), 421–433.
949	Codillo, E. A., Klein, F., & Marschall, H. R. (2022). Preferential formation of chlorite
950	over talc during si-metasomatism of ultramafic rocks in subduction zones.
951	Geophysical Research Letters, 49 (19), e2022GL100218.
952	Condit, C. B., & French, M. E. (2022). Geologic evidence of lithostatic pore fluid pressures at
953	the base of the subduction seismogenic zone. Geophysical Research Letters, 49(12),
954	e2022GL098862.
955	Condit, C. B., Guevara, V. E., Delph, J. R., & French, M. E. (2020). Slab dehydration in warm
956	subduction zones at depths of episodic slip and tremor. Earth and Planetary Science
957	Letters, 552, 116601.
958	Connolly, J. A. D. (2005). Computation of phase equilibria by linear programming: A tool for
959	geodynamic modeling and its application to subduction zone decarbonation. Earth
960	and Planetary Science Letters, 236(1–2), 524–541.
961	https://doi.org/10.1016/j.epsl.2005.04.033
962	Conrad, C. P., & Hager, B. H. (1999). The thermal evolution of an Earth with strong
963	subduction zones. Geophysical Research Letters, 26(19), 3041–3044.
964	https://doi.org/https://doi.org/10.1029/1999GL005397
965	Davies, J. H. (1999). The role of hydraulic fractures and intermediate-depth earthquakes in
966	generating subduction-zone magmatism. <i>Nature</i> , 398(6723), 142–145.
967	https://doi.org/10.1038/18202
968	Dengo, C. A., & Logan, J. M. (1981). Implications of the mechanical and frictional behavior of
969	serpentinite to seismogenic faulting. Journal of Geophysical Research: Solid Earth,
970	86(B11), 10771–10782. https://doi.org/https://doi.org/10.1029/JB086iB11p10771

971	Douglas, D., Codillo, E., Epstein, G. S., Seltzer, C., Strobl, L., & Mallick, E. (2023). Geodynamic
972	Constraints on the Stability of Forearc Serpentinite in the Cold Nose of the Mantle
973	Wedge. In AGU Fall Meeting Abstracts (Vol. 2023, pp. DI21C0023).
974	Dragovic, B., Angiboust, S., & Tappa, M. J. (2020). Petrochronological close-up on the
975	thermal structure of a paleo-subduction zone (W. Alps). Earth and Planetary Science
976	Letters, 547, 116446. https://doi.org/https://doi.org/10.1016/j.epsl.2020.116446
977	Easthouse, G., Hoover, W., Teng, FZ., Condit, C., Pike, C., Wang, ZZ., Poulaki, E.
978	(2025). Formation of talc in the subduction interface: Mg isotopes demonstrate mg
979	loss over si gain. <i>Geology</i> , 53 (5), 398–403.
980	England, P. C., & Richardson, S. W. (1977). The influence of erosion upon the mineral facies
981	of rocks from different metamorphic environments. Journal of the Geological
982	Society, 134(2), 201–213. https://doi.org/10.1144/gsjgs.134.2.0201
983	England, P. C., & Smye, A. J. (2023). Metamorphism and deformation on subduction
984	interfaces: 1. Physical framework. Geochemistry, Geophysics, Geosystems, 24(1),
985	e2022GC010644.
986	Epstein, G. S., Bebout, G. E., & Angiboust, S. (2021). Fluid and mass transfer along transient
987	subduction interfaces in a deep paleo-accretionary wedge (western alps). Chemical
988	Geology, 559, 119920.
989	Epstein, G. S., Condit, C. B., Stoner, R. K., Holt, A. F., & Guevara, V. E. (2024). Evolving
990	subduction zone thermal structure drives extensive forearc mantle wedge hydration.
991	AGU Advances, 5(4), e2023AV001121.
992	Escartin, J., Hirth, G., & Evans, B. (1997). Effects of serpentinization on the lithospheric
993	strength and the style of normal faulting at slow-spreading ridges. Earth and
994	Planetary Science Letters, 151(3–4), 181–189.
995	Faccenda, M., Gerya, T. V., Mancktelow, N. S., & Moresi, L. (2012). Fluid flow during
996	slab unbending and dehydration: Implications for intermediate-depth seismicity, slab
997	weakening and deep water recycling. Geochemistry, Geophysics, Geosystems, 13 (1).
998	Faccenna, C., Becker, T. W., Lucente, F. P., Jolivet, L., & Rossetti, F. (2001). History of
999	subduction and back arc extension in the Central Mediterranean. Geophysical
1000	Journal International, 145(3), 809–820.

1001	Fildes, R. A., & Billen, M. I. (2025). Linking visco-elasto-plastic modeling of recent slab
1002	deformation to present-day deep earthquakes. Journal of Geophysical Research:
1003	Solid Earth, 130(3), e2024JB029678.
1004	Frost, H. J., and M. F. Ashby (1982), Deformation Mechanism Maps, 167 pp., Pergamon,
1005	New York.
1006	Fryer, P., Wheat, C. G., & Mottl, M. J. (1999). Mariana blueschist mud volcanism:
1007	Implications for conditions within the subduction zone. <i>Geology</i> , 27(2), 103–106.
1008	https://doi.org/10.1130/0091-7613(1999)027<0103:MBMVIF>2.3.CO;2
1009	Furukawa, Y. (1993). Depth of the decoupling plate interface and thermal structure under
1010	arcs. Journal of Geophysical Research: Solid Earth, 98(B11), 20005–20013.
1011	Gao, X., & Wang, K. (2014). Strength of stick-slip and creeping subduction megathrusts from
1012	heat flow observations. Science, 345(6200), 1038–1041.
1013	Gavrilenko, M., Krawczynski, M., Ruprecht, P., Li, W., & Catalano, J. G. (2019). The quench
1014	control of water estimates in convergent margin magmas. American Mineralogist,
1015	104(7), 936–948. https://doi.org/doi:10.2138/am-2019-6735
1016	Gerya, T. V, & Meilick, F. I. (2011). Geodynamic regimes of subduction under an active
1017	margin: effects of rheological weakening by fluids and melts. Journal of Metamorphic
1018	Geology, 29(1), 7-31. https://doi.org/https://doi.org/10.1111/j.1525-
1019	1314.2010.00904.x
1020	Gerya, T. V, Connolly, J. A. D., & Yuen, D. A. (2008). Why is terrestrial subduction one-sided?
1021	Geology, 36(1), 43-46. https://doi.org/10.1130/G24060A.1
1022	Gerya, T. V, Stöckhert, B., & Perchuk, A. L. (2002). Exhumation of high-pressure
1023	metamorphic rocks in a subduction channel: A numerical simulation. Tectonics,
1024	21(6), 1–6.
1025	Gerya, T., & Stöckhert, B. (2006). Two-dimensional numerical modeling of tectonic and
1026	metamorphic histories at active continental margins. International Journal of Earth
1027	Sciences, 95(2), 250–274. https://doi.org/10.1007/s00531-005-0035-9
1028	Glerum, A., Thieulot, C., Fraters, M., Blom, C., & Spakman, W. (2018). Nonlinear
1029	viscoplasticity in ASPECT: benchmarking and applications to subduction. Solid Earth,
1030	9(2), 267–294. https://doi.org/10.5194/se-9-267-2018
1031	Gorczyk, W., Willner, A. P., Gerya, T. V, Connolly, J. A. D., & Burg, JP. (2007). Physical
1032	controls of magmatic productivity at Pacific-type convergent margins: Numerical

1033	modelling. Physics of the Earth and Planetary Interiors, 163(1), 209–232.
1034	https://doi.org/https://doi.org/10.1016/j.pepi.2007.05.010
1035	Hacker, B. R. (2008). H <sub>2</sub> O subduction beyond arcs. <i>Geochemistry, Geophysics, Geosystems</i> ,
1036	9(3). https://doi.org/10.1029/2007GC001707
1037	Hacker, B. R., & Christie, J. M. (1990). Brittle/ductile and plastic/cataclastic transitions in
1038	experimentally deformed and metamorphosed amphibolite. The Brittle-Ductile
1039	Transition in Rocks, 56, 127–147.
1040	Halpaap, F., Rondenay, S., Perrin, A., Goes, S., Ottemöller, L., Austrheim, H., et al. (2019).
1041	Earthquakes track subduction fluids from slab source to mantle wedge sink. Science
1042	Advances, 5(4), eaav7369.
1043	Hamilton, D. L., Burnham, C. W., & Osborn, E. F. (1964). The Solubility of Water and Effects
1044	of Oxygen Fugacity and Water Content on Crystallization in Mafic Magmas1. Journal
1045	of Petrology, 5(1), 21–39. https://doi.org/10.1093/petrology/5.1.21
1046	Heister, T., Dannberg, J., Gassmöller, R., & Bangerth, W. (2017). High accuracy mantle
1047	convection simulation through modern numerical methods – II: realistic models and
1048	problems. Geophysical Journal International, 210(2), 833–851.
1049	https://doi.org/10.1093/gji/ggx195
1050	Hernández-Uribe, D., & Palin, R. M. (2019). A revised petrological model for subducted
1051	oceanic crust: Insights from phase equilibrium modelling. Journal of Metamorphic
1052	<i>Geology, 37</i> (6), 745–768.
1053	Hilairet, N., & Reynard, B. (2009). Stability and dynamics of serpentinite layer in subduction
1054	zone. Tectonophysics, 465(1), 24–29.
1055	https://doi.org/https://doi.org/10.1016/j.tecto.2008.10.005
1056	Hilairet, N., Reynard, B., Wang, Y., Daniel, I., Merkel, S., Nishiyama, N., & Petitgirard, S.
1057	(2007). High-pressure creep of serpentine, interseismic deformation, and initiation of
1058	subduction. <i>Science</i> , <i>318</i> (5858), 1910–1913.
1059	Hirth, G., & Kohlstedt, D. (2003). Rheology of the upper mantle and the mantle wedge: A
1060	view from the experimentalists. In J. Eiler (Ed.), Geophysical Monograph Series (Vol.
1061	138, pp. 83–105). Washington, D. C.: American Geophysical Union. Retrieved from
1062	http://www.agu.org/books/gm/v138/138GM06/138GM06.shtml

1063	Hirth, G., Teyssier, C., & Dunlap, J. W. (2001). An evaluation of quartzite flow laws based on
1064	comparisons between experimentally and naturally deformed rocks. International
1065	Journal of Earth Sciences, 90(1), 77–87. https://doi.org/10.1007/s005310000152
1066	Holland, T. J. B., & Powell, R. (2011). An improved and extended internally consistent
1067	thermodynamic dataset for phases of petrological interest, involving a new equation
1068	of state for solids. Journal of Metamorphic Geology, 29(3), 333–383.
1069	Holt, A. F., & Condit, C. B. (2021). Slab temperature evolution over the lifetime of a
1070	subduction zone. Geochemistry, Geophysics, Geosystems, 22(6), e2020GC009476.
1071	Horn, H. M., & Deere, D. U. (1962). Frictional characteristics of minerals. <i>Geotechnique</i> ,
1072	<i>12</i> (4), 319–335.
1073	Hyndman, R. D., & Peacock, S. M. (2003). Serpentinization of the forearc mantle. Earth and
1074	Planetary Science Letters, 212(3–4), 417–432.
1075	Isacks, B., & Molnar, P. (1971). Distribution of stresses in the descending lithosphere from a
1076	global survey of focal-mechanism solutions of mantle earthquakes. Reviews of
1077	Geophysics, 9(1), 103–174.
1078	Isacks, B., Oliver, J., & Sykes, L. R. (1968). Seismology and the new global tectonics. <i>Journal</i>
1079	of Geophysical Research, 73(18), 5855–5899.
1080	Ito, E., Harris, D. M., & Anderson, A. T. (1983). Alteration of oceanic crust and geologic
1081	cycling of chlorine and water. Geochimica et Cosmochimica Acta, 47(9), 1613–1624.
1082	https://doi.org/https://doi.org/10.1016/0016-7037(83)90188-6
1083	Iwamori, H. (2007). Transportation of H2O beneath the Japan arcs and its implications for
1084	global water circulation. Chemical Geology, 239(3), 182-198.
1085	https://doi.org/https://doi.org/10.1016/j.chemgeo.2006.08.011
1086	Jagoutz, O., Royden, L., Holt, A. F., & Becker, T. W. (2015). Anomalously fast convergence of
1087	India and Eurasia caused by double subduction. <i>Nature Geoscience</i> , 8(6), 475–478.
1088	Jarrard, R. D. (2003). Subduction fluxes of water, carbon dioxide, chlorine, and potassium.
1089	Geochemistry, Geophysics, Geosystems, 4(5).
1090	Julve, J., Barbot, S., Moreno, M., Tassara, A., Araya, R., Catalán, N., et al. (2024). Recurrence
1091	time and size of Chilean earthquakes influenced by geological structure. Nature
1092	Geoscience, 17(1), 79-87. https://doi.org/10.1038/s41561-023-01327-8
1093	Kameyama, M., Yuen, D. A., & Karato, SI. (1999). Thermal-mechanical effects of low-
1094	temperature plasticity (the Peierls mechanism) on the deformation of a viscoelastic

1095	shear zone. Earth and Planetary Science Letters, 168(1), 159–172.
1096	https://doi.org/https://doi.org/10.1016/S0012-821X(99)00040-0
1097	Karato, S. I., & Wu, P. (1993). Rheology of the upper mantle: A synthesis. Science, 260, 771–
1098	778.
1099	Katz, R. F., Spiegelman, M., & Langmuir, C. H. (2003). A new parameterization of hydrous
1100	mantle melting. Geochemistry, Geophysics, Geosystems, 4(9).
1101	https://doi.org/10.1029/2002GC000433
1102	Kawano, S., Katayama, I., & Okazaki, K. (2011). Permeability anisotropy of serpentinite and
1103	fluid pathways in a subduction zone. Geology, 39(10), 939–942.
1104	Kerswell, B. C., Kohn, M. J., & Gerya, T. V. (2021). Backarc lithospheric thickness and
1105	serpentine stability control slab-mantle coupling depths in subduction zones.
1106	Geochemistry, Geophysics, Geosystems, 22(6), e2020GC009304.
1107	Kimura, G., & Ludden, J. (1995). Peeling oceanic crust in subduction zones. <i>Geology</i> , 23(3),
1108	217–220.
1109	Kincaid, C., & Sacks, I. S. (1997). Thermal and dynamical evolution of the upper mantle in
1110	subduction zones. Journal of Geophysical Research: Solid Earth, 102(B6), 12295—
1111	12315. https://doi.org/https://doi.org/10.1029/96JB03553
1112	King, S. D., & Hager, B. H. (1990). The relationship between plate velocity and trench
1113	viscosity in Newtonian and power-law subduction calculations. Geophysical Research
1114	Letters, 17(13), 2409–2412.
1115	https://doi.org/https://doi.org/10.1029/GL017i013p02409
1116	Kirby, S. H., Stein, S., Okal, E. A., & Rubie, D. C. (1996). Metastable mantle phase
1117	transformations and deep earthquakes in subducting oceanic lithosphere. Reviews of
1118	Geophysics, 34(2), 261–306.
1119	Klein, B. Z., & Behn, M. D. (2025). The impact of mélange formation on the rheology
1120	and h2o budget of the subduction zone interface, with implications for diapir
1121	nucleation. Geophysical Research Letters, 52 (7), e2024GL113049.
1122	Kocks, U. F., A. S. Argon, and M. F. Ashby (1975), Thermodynamics and Kinetics of Slip, 291
1123	pp., Pergamon, Oxford.
1124	Kronbichler, M., Heister, T., & Bangerth, W. (2012). High Accuracy Mantle Convection
1125	Simulation through Modern Numerical Methods. Geophysical Journal International,
1126	191, 12-29. https://doi.org/10.1111/j.1365-246X.2012.05609.x

1127	Lallemand, S., Heuret, A., & Boutelier, D. (2005). On the relationships between slab dip,
1128	back-arc stress, upper plate absolute motion, and crustal nature in subduction zones.
1129	Geochemistry, Geophysics, Geosystems, 6(9).
1130	Lamb, S. (2006). Shear stresses on megathrusts: Implications for mountain building behind
1131	subduction zones. Journal of Geophysical Research: Solid Earth, 111(B7).
1132	Lamb, S., & Davis, P. (2003). Cenozoic climate change as a possible cause for the rise of the
1133	Andes. Nature, 425(6960), 792–797. https://doi.org/10.1038/nature02049
1134	Li, ZH., Gerya, T., & Connolly, J. A. D. (2019). Variability of subducting slab morphologies in
1135	the mantle transition zone: Insight from petrological-thermomechanical modeling.
1136	Earth-Science Reviews, 196, 102874.
1137	https://doi.org/https://doi.org/10.1016/j.earscirev.2019.05.018
1138	Lindquist, P. C., Condit, C. B., Hoover, W. F., Hernández-Uribe, D., & Guevara, V. E. (2023).
1139	Metasomatism and Slow Slip: Talc Production Along the Flat Subduction Plate
1140	Interface Beneath Mexico (Guerrero). Geochemistry, Geophysics, Geosystems, 24(8),
1141	e2023GC010981. https://doi.org/https://doi.org/10.1029/2023GC010981
1142	Magni, V., Bouilhol, P., & Van Hunen, J. (2014). Deep water recycling through time.
1143	Geochemistry, Geophysics, Geosystems, 15(11), 4203–4216.
1144	Menant, A., Angiboust, S., & Gerya, T. (2019). Stress-driven fluid flow controls long-term
1145	megathrust strength and deep accretionary dynamics. Scientific Reports, 9(1), 9714.
1146	Mitchell, A. L., Gaetani, G. A., O'Leary, J. A., & Hauri, E. H. (2017). H2O solubility in basalt at
1147	upper mantle conditions. Contributions to Mineralogy and Petrology, 172(10), 85.
1148	https://doi.org/10.1007/s00410-017-1401-x
1149	Molnar, P., & England, P. (1990). Temperatures, heat flux, and frictional stress near major
1150	thrust faults. Journal of Geophysical Research: Solid Earth, 95(B4), 4833–4856.
1151	https://doi.org/https://doi.org/10.1029/JB095iB04p04833
1152	Moore, D. E., Lockner, D. A., Ma, S., Summers, R., & Byerlee, J. D. (1997). Strengths of
1153	serpentinite gouges at elevated temperatures. Journal of Geophysical Research: Solid
1154	Earth, 102(B7), 14787–14801. https://doi.org/https://doi.org/10.1029/97JB00995
1155	Moore, D. E., Lockner, D. A., Summers, R., Shengli, M. A., & Byerlee, J. D. (1996). Strength of
1156	chrysotile-serpentinite gouge under hydrothermal conditions: Can it explain a weak
1157	San Andreas fault? <i>Geology, 24</i> (11), 1041–1044.

1158	Moore, D. E., & Lockner, D. A. (2004). Crystallographic controls on the frictional behavior of
1159	dry and water-saturated sheet structure minerals. Journal of Geophysical Research:
1160	Solid Earth, 109(B3).
1161	Moreno, M., Haberland, C., Oncken, O., Rietbrock, A., Angiboust, S., & Heidbach, O. (2014).
1162	Locking of the Chile subduction zone controlled by fluid pressure before the 2010
1163	earthquake. Nature Geoscience, 7(4), 292–296.
1164	Nakao, A., Iwamori, H., & Nakakuki, T. (2016). Effects of water transportation on subduction
1165	dynamics: Roles of viscosity and density reduction. Earth and Planetary Science
1166	Letters, 454, 178–191. https://doi.org/https://doi.org/10.1016/j.epsl.2016.08.016
1167	Nakao, A., Iwamori, H., Nakakuki, T., Suzuki, Y. J., & Nakamura, H. (2018). Roles of Hydrous
1168	Lithospheric Mantle in Deep Water Transportation and Subduction Dynamics.
1169	Geophysical Research Letters, 45(11), 5336–5343.
1170	https://doi.org/https://doi.org/10.1029/2017GL076953
1171	Nikolaeva, K., Gerya, T. V, & Connolly, J. A. D. (2008). Numerical modelling of crustal growth
1172	in intraoceanic volcanic arcs. Physics of the Earth and Planetary Interiors, 171(1–4),
1173	336–356.
1174	Oyanagi, R., & Okamoto, A. (2024). Subducted carbon weakens the forearc mantle wedge in
1175	a warm subduction zone. Nature Communications, 15(1), 7159.
1176	https://doi.org/10.1038/s41467-024-51476-6
1177	Peacock, S. M. (1990). Numerical simulation of metamorphic pressure-temperature-time
1178	paths and fluid production in subducting slabs. <i>Tectonics</i> , 9(5), 1197–1211.
1179	Peacock, S. M. (1987). Creation and preservation of subduction-related inverted
1180	metamorphic gradients. Journal of Geophysical Research: Solid Earth, 92(B12),
1181	12763–12781.
1182	Peacock, S. M. (1992). Blueschist-facies metamorphism, shear heating, and P-T-t paths in
1183	subduction shear zones. Journal of Geophysical Research: Solid Earth, 97(B12),
1184	17693-17707. https://doi.org/https://doi.org/10.1029/92JB01768
1185	Peacock, S. M., Christensen, N. I., Bostock, M. G., & Audet, P. (2011). High pore pressures
1186	and porosity at 35 km depth in the Cascadia subduction zone. Geology, 39(5), 471–
1187	474.

1188	Peacock, S. M., & Wang, K. (2021). On the stability of talc in subduction zones: a possible
1189	control on the maximum depth of decoupling between the subducting plate and
1190	mantle wedge. Geophysical Research Letters, 48(17), e2021GL094889.
1191	Penniston-Dorland, S. C., Kohn, M. J., & Manning, C. E. (2015). The global range of
1192	subduction zone thermal structures from exhumed blueschists and eclogites: Rocks
1193	are hotter than models. Earth and Planetary Science Letters, 428, 243–254.
1194	https://doi.org/10.1016/j.epsl.2015.07.031
1195	Penniston-Dorland, S. C., Wada, I., Raia, N. H., Steele, A., Bullock, E. S., Zhou, X., et al. (2025).
1196	Constraining the thermal structure of the subduction plate interface: Coupled
1197	petrologic and geodynamic study of high-pressure rocks of New Caledonia. Earth and
1198	Planetary Science Letters, 652, 119172.
1199	https://doi.org/https://doi.org/10.1016/j.epsl.2024.119172
1200	Pitzer, K. S., & Sterner, S. M. (1994). Equations of state valid continuously from zero to
1201	extreme pressures for H2O and CO2. The Journal of Chemical Physics, 101(4), 3111–
1202	3116. https://doi.org/10.1063/1.467624
1203	Plank, T., & Langmuir, C. H. (1998). The chemical composition of subducting sediment and
1204	its consequences for the crust and mantle. Chemical Geology, 145(3-4), 325-394.
1205	https://doi.org/10.1016/S0009-2541(97)00150-2
1206	Platt, J. P. (1975). Metamorphic and deformational processes in the Franciscan Complex,
1207	California: Some insights from the Catalina Schist terrane. Geological Society of
1208	America Bulletin, 86(10), 1337–1347.
1209	Podolefsky, N. S., Zhong, S., & McNamara, A. K. (2004). The anisotropic and rheological
1210	structure of the oceanic upper mantle from a simple model of plate shear.
1211	Geophysical Journal International, 158(1), 287–296.
1212	Pusok, A. E., Stegman, D. R., & Kerr, M. (2022). The effect of low-viscosity sediments on the
1213	dynamics and accretionary style of subduction margins. Solid Earth, 13(9), 1455–
1214	1473. https://doi.org/10.5194/se-13-1455-2022.
1215	Putnis, A., & Austrheim, H. (2010). Fluid-induced processes: metasomatism and
1216	metamorphism. <i>Geofluids</i> , 10 (1-2), 254–269.
1217	Raleigh, C. B., & Paterson, M. S. (1965). Experimental deformation of serpentinite and its
1218	tectonic implications. Journal of Geophysical Research, 70(16), 3965–3985.

1219	Ranero, C. R., Phipps Morgan, J., McIntosh, K., & Reichert, C. (2003). Bending-related
1220	faulting and mantle serpentinization at the Middle America trench. Nature,
1221	425(6956), 367–373. https://doi.org/10.1038/nature01961
1222	Reinen, L. A., Weeks, J. D., & Tullis, T. E. (1994). The frictional behavior of lizardite and
1223	antigorite serpentinites: Experiments, constitutive models, and implications for
1224	natural faults. Pure and Applied Geophysics, 143, 317–358.
1225	Ring, U., Brandon, M. T., Willett, S. D., & Lister, G. S. (1999). Exhumation processes.
1226	Geological Society, London, Special Publications, 154(1), 1–27.
1227	https://doi.org/10.1144/GSL.SP.1999.154.01.01
1228	Ritter, S., Balázs, A., Ribeiro, J., & Gerya, T. (2024). Magmatic fingerprints of subduction
1229	initiation and mature subduction: numerical modelling and observations from the
1230	Izu-Bonin-Mariana system. Frontiers in Earth Science, Volume 12-2024.
1231	https://doi.org/10.3389/feart.2024.1286468
1232	Ian Rose, Bruce Buffett, and Timo Heister. 2017. "Stability and Accuracy of Free Surface
1233	Time Integration in Viscous Flows." Physics of the Earth and Planetary Interiors 262
1234	(January): 90–100. https://doi:10.1016/j.pepi.2016.11.007.
1235	Rowe, C. D., Moore, J. C., Remitti, F., & Scientists, I. E. 343/343T. (2013). The thickness of
1236	subduction plate boundary faults from the seafloor into the seismogenic zone.
1237	Geology, 41(9), 991–994.
1238	Rüpke, L. H., Morgan, J. P., Hort, M., & Connolly, J. A. D. (2004). Serpentine and the
1239	subduction zone water cycle. <i>Earth and Planetary Science Letters</i> , 223(1–2), 17–34.
1240	Rutter, E. H. (1976). A discussion on natural strain and geological structure-the kinetics of
1241	rock deformation by pressure solution. Philosophical Transactions of the Royal
1242	Society of London. Series A, Mathematical and Physical Sciences, 283(1312), 203-
1243	219.
1244	Savov, I. P., Ryan, J. G., D'Antonio, M., & Fryer, P. (2007). Shallow slab fluid release across
1245	and along the Mariana arc-basin system: Insights from geochemistry of serpentinized
1246	peridotites from the Mariana fore arc. Journal of Geophysical Research: Solid Earth,
1247	<i>112</i> (B9).
1248	Scambelluri, M., Cannaò, E., & Gilio, M. (2019). The water and fluid-mobile element cycles
1249	during serpentinite subduction. A review. European Journal of Mineralogy, 31(3),
1250	405–428.

1251	Scambelluri, M., & Tonarini, S. (2012). Boron isotope evidence for shallow fluid transfer
1252	across subduction zones by serpentinized mantle. Geology, 40(10), 907–910.
1253	https://doi.org/10.1130/G33233.1
1254	Schmidt, M. W., & Poli, S. (1998). Experimentally based water budgets for dehydrating slabs
1255	and consequences for arc magma generation. Earth and Planetary Science Letters,
1256	163(1), 361–379. https://doi.org/https://doi.org/10.1016/S0012-821X(98)00142-3
1257	Schwartz, S., Allemand, P., & Guillot, S. (2001). Numerical model of the effect of
1258	serpentinites on the exhumation of eclogitic rocks: insights from the Monviso
1259	ophiolitic massif (Western Alps). <i>Tectonophysics</i> , 342(1–2), 193–206.
1260	Scuderi, M. M., & Carpenter, B. M. (2022). Frictional stability and hydromechanical coupling
1261	of serpentinite-bearing fault gouge. Geophysical Journal International, 231(1), 290–
1262	305.
1263	Sdrolias, M., & Müller, R. D. (2006). Controls on back-arc basin formation. <i>Geochemistry</i> ,
1264	Geophysics, Geosystems, 7(4).
1265	Shreve, R. L., & Cloos, M. (1986). Dynamics of sediment subduction, melange formation, and
1266	prism accretion. Journal of Geophysical Research: Solid Earth, 91(B10), 10229–10245
1267	Stein, C. A., & Stein, S. (1992). A model for the global variation in oceanic depth and heat
1268	flow with lithospheric age. Nature, 359(6391), 123–129.
1269	Stoner, R.K., Holt, A.F., Epstein, G.S., Condit, C.B., & Guevara, V.E. (2025).
1270	ryanstoner1/aspect: v0.1.3-alpha (v0.1.3-alpha). Zenodo.
1271	https://doi.org/10.5281/zenodo.15345801
1272	Takahashi, M., Uehara, SI., Mizoguchi, K., Shimizu, I., Okazaki, K., & Masuda, K. (2011). On
1273	the transient response of serpentine (antigorite) gouge to stepwise changes in slip
1274	velocity under high-temperature conditions. Journal of Geophysical Research: Solid
1275	Earth, 116(B10).
1276	Tarling, M. S., Smith, S. A. F., Scott, J. M., Rooney, J. S., Viti, C., & Gordon, K. C. (2019). The
1277	internal structure and composition of a plate-boundary-scale serpentinite shear
1278	zone: the Livingstone Fault, New Zealand. Solid Earth, 10(4), 1025–1047.
1279	Tatsumi, Y. (1986). Formation of the volcanic front in subduction zones. Geophysical
1280	Research Letters, 13(8), 717–720.
1281	Tatsumi, Y., & Eggins, S. (1995). Subduction zone magmatism. In Subduction zone
1282	magmatism. Blackwell Science; Frontiers in Earth Sciences.

1283	Tesei, T., Harbord, C. W. A., De Paola, N., Collettini, C., & Viti, C. (2018). Friction of
1284	Mineralogically Controlled Serpentinites and Implications for Fault Weakness.
1285	Journal of Geophysical Research: Solid Earth, 123(8), 6976–6991.
1286	https://doi.org/https://doi.org/10.1029/2018JB016058
1287	Tonarini, S., Leeman, W. P., & Leat, P. T. (2011). Subduction erosion of forearc mantle
1288	wedge implicated in the genesis of the South Sandwich Island (SSI) arc: evidence
1289	from boron isotope systematics. Earth and Planetary Science Letters, 301(1–2), 275–
1290	284.
1291	Tulley, C. J., ten Thij, L., Niemeijer, A. R., Hamers, M. F., & Fagereng, Å. (2024). Activation of
1292	dissolution-precipitation creep causes weakening and viscous behavior in
1293	experimentally deformed antigorite. Journal of Geophysical Research: Solid Earth,
1294	<i>129</i> (8), e2024JB029053.
1295	Turino, V., & Holt, A. F. (2024). Spatio-temporal variability in slab temperature within
1296	dynamic 3-D subduction models. Geophysical Journal International, 236(3), 1484–
1297	1498. https://doi.org/10.1093/gji/ggad489
1298	Ueda, K., Gerya, T., & Sobolev, S. V. (2008). Subduction initiation by thermal–chemical
1299	plumes: Numerical studies. Physics of the Earth and Planetary Interiors, 171(1), 296-
1300	312. https://doi.org/https://doi.org/10.1016/j.pepi.2008.06.032
1301	van Keken, P. E., Hacker, B. R., Syracuse, E. M., & Abers, G. A. (2011). Subduction factory: 4.
1302	Depth-dependent flux of H <sub>2</sub> O from subducting slabs worldwide. <i>Journal of</i>
1303	Geophysical Research: Solid Earth, 116(B1).
1304	Wada, I., Behn, M. D., & Shaw, A. M. (2012). Effects of heterogeneous hydration in the
1305	incoming plate, slab rehydration, and mantle wedge hydration on slab-derived $\ensuremath{\text{H}_2\text{O}}$
1306	flux in subduction zones. Earth and Planetary Science Letters, 353, 60–71.
1307	Wada, I., & Wang, K. (2009). Common depth of slab-mantle decoupling: Reconciling
1308	diversity and uniformity of subduction zones. Geochemistry, Geophysics,
1309	Geosystems, 10(10).
1310	Wada, I., Wang, K., He, J., & Hyndman, R. D. (2008). Weakening of the subduction interface
1311	and its effects on surface heat flow, slab dehydration, and mantle wedge
1312	serpentinization. Journal of Geophysical Research: Solid Earth, 113(B4).

1313	Wang, K., Hyndman, R. D., & Yamano, M. (1995). Thermal regime of the Southwest Japan
1314	subduction zone: effects of age history of the subducting plate. Tectonophysics,
1315	<i>248</i> (1–2), 53–69.
1316	Wilson, C. R., Spiegelman, M., van Keken, P. E., & Hacker, B. R. (2014). Fluid flow in
1317	subduction zones: The role of solid rheology and compaction pressure. Earth and
1318	Planetary Science Letters, 401, 261–274.
1319	https://doi.org/https://doi.org/10.1016/j.epsl.2014.05.052
1320	Zhang, J., & Green, H. W. (2007). Experimental investigation of eclogite rheology and its
1321	fabrics at high temperature and pressure. Journal of Metamorphic Geology, 25(2),
1322	97–115.
1323	Zhou, X., & Wada, I. (2021). Differentiating induced versus spontaneous subduction
1324	initiation using thermomechanical models and metamorphic soles. Nature
1325	Communications, 12(1), 4632.
וחחר	References From the Supporting Information
1326	References From the Supporting information
1327	Amiguet, E., Van De Moortèle, B., Cordier, P., Hilairet, N., & Reynard, B. (2014). Deformation
1328	mechanisms and rheology of serpentines in experiments and in nature. Journal of
1329	Geophysical Research: Solid Earth, 119(6), 4640–4655.
1330	https://doi.org/https://doi.org/10.1002/2013JB010791
1331	Auzanneau, E., Schmidt, M. W., Vielzeuf, D., & Connolly, J. A. D. (2010). Titanium in
1332	phengite: a geobarometer for high temperature eclogites. Contributions to Mineralogy
1333	and Petrology, 159, 1–24. https://doi.org/10.1007/s00410-009-0412-7
1334	Behnsen, J., & Faulkner, D. R. (2012). The effect of mineralogy and effective normal stress
1335	on frictional strength of sheet silicates. <i>Journal of Structural Geology, 42,</i> 49–61.
1336	Behr, W. M., & Platt, J. P. (2013). Rheological evolution of a Mediterranean subduction
1337	complex. Journal of Structural Geology, 54, 136–155.
1338	Burdette, E., & Hirth, G. (2022). Creep rheology of antigorite: Experiments at subduction
1339	zone conditions. Journal of Geophysical Research: Solid Earth, 127(7), e2022JB024260.
1340	Carpenter, B. M., Marone, C., & Saffer, D. M. (2009). Frictional behavior of materials in the
1341	3D SAFOD volume. Geophysical Research Letters, 36(5).
1342	https://doi.org/https://doi.org/10.1029/2008GL036660

Chernak, L. J., & Hirth, G. (2010). Deformation of antigorite serpentinite at high temperature 1343 and pressure. Earth and Planetary Science Letters, 296(1–2), 23–33. 1344 Coggon, R. and Holland, T. J. B. (2002), Mixing properties of phengitic micas and revised 1345 1346 garnet-phengite thermobarometers. Journal of Metamorphic Geology, 20: 683-696. https://doi.org/10.1046/j.1525-1314.2002.00395.x 1347 Connolly, J. A. D., Trommsdorff, V. (1991). Petrogenetic grids for metacarbonate rocks: 1348 pressure-temperature phase-diagram projection for mixed-volatile 1349 systems. Contributions to Mineralogy and Petrology, 108, 93–105. 1350 https://doi.org/10.1007/BF00307329 1351 1352 Dengo, C. A., & Logan, J. M. (1981). Implications of the mechanical and frictional behavior of 1353 serpentinite to seismogenic faulting. Journal of Geophysical Research: Solid Earth, 1354 86(B11), 10771–10782. https://doi.org/https://doi.org/10.1029/JB086iB11p10771 1355 Escartin, J., Hirth, G., & Evans, B. (1997). Effects of serpentinization on the lithospheric 1356 strength and the style of normal faulting at slow-spreading ridges. Earth and Planetary 1357 Science Letters, 151(3-4), 181-189. Fildes, R. A., & Billen, M. I. (2025). Linking visco-elasto-plastic modeling of recent slab 1358 1359 deformation to present-day deep earthquakes. Journal of Geophysical Research: Solid Earth, 130(3), e2024JB029678. 1360 Fuhrman, M. L., & Lindsley, D. H. (1988). Ternary-feldspar modeling and thermometry. 1361 American Mineralogist, 73(3-4), 201-215. https://doi.org/10.2138/am-1988-3-421 1362 Green, E. C. R., Holland, T. J. B., & Powell, R. (2007). An order-disorder model for omphacitic 1363 1364 pyroxenes in the system jadeite-diopsidehedenbergite- acmite, with applications to eclogitic rocks. American Mineralogist, 92(7), 1181-1365 1189. https://doi.org/10.2138/am.2007.2401 1366 Green, E. C. R., White, R. W., Diener, J. F. A., Powell, R., Holland, T. J. B. and Palin, R. M. 1367 (2016), Activity-composition relations for the calculation of partial melting equilibria in 1368 metabasic rocks. Journal of Metamorphic Geology, 34: 845-1369 869. https://doi.org/10.1111/jmg.12211 1370 Hilairet, N., Reynard, B., Wang, Y., Daniel, I., Merkel, S., Nishiyama, N., & Petitgirard, S. 1371 (2007). High-pressure creep of serpentine, interseismic deformation, and initiation of 1372 1373 subduction. *Science*, *318*(5858), 1910–1913.

- Holland, T. J. B., Green, E. C. R., & Powell, R. (2018). Melting of peridotites through to
- granites: a simple thermodynamic model in the system KNCFMASHTOCr. *Journal of*
- 1376 *Petrology, 59*(5), 881-900.
- Holland, T. J. B., Hudson, N. F., Powell, R., & Harte, B. (2013). New thermodynamic models
- and calculated phase equilibria in NCFMAS for basic and ultrabasic compositions
- through the transition zone into the uppermost lower mantle. *Journal of*
- 1380 *Petrology*, *54*(9), 1901-1920.
- Holland, T. J. B., & Powell, R. (2011). An improved and extended internally consistent
- thermodynamic dataset for phases of petrological interest, involving a new equation of
- state for solids. *Journal of Metamorphic Geology*, 29(3), 333-383.
- Jennings, E. S., & Holland, T. J. B. (2015). A simple thermodynamic model for melting of
- peridotite in the system NCFMASOCr. *Journal of Petrology*, *56*(5), 869-892.
- Kawano, S., Katayama, I., & Okazaki, K. (2011). Permeability anisotropy of serpentinite and
- fluid pathways in a subduction zone. *Geology*, *39*(10), 939–942.
- Moore, D. E., Lockner, D. A., Ma, S., Summers, R., & Byerlee, J. D. (1997). Strengths of
- serpentinite gouges at elevated temperatures. Journal of Geophysical Research: Solid
- 1390 *Earth*, *102*(B7), 14787–14801. https://doi.org/https://doi.org/10.1029/97JB00995
- Moore, D. E., Lockner, D. A., Summers, R., Shengli, M. A., & Byerlee, J. D. (1996). Strength of
- chrysotile-serpentinite gouge under hydrothermal conditions: Can it explain a weak San
- 1393 Andreas fault? *Geology*, *24*(11), 1041–1044.
- Moore, D. E., & Lockner, D. A. (2004). Crystallographic controls on the frictional behavior of
- dry and water-saturated sheet structure minerals. *Journal of Geophysical Research:*
- 1396 *Solid Earth, 109*(B3).
- Padrón-Navarta, J. A., Sánchez-Vizcaíno, V. L., Hermann, J., Connolly, J. A., Garrido, C. J.,
- Gómez-Pugnaire, M. T., & Marchesi, C. (2013). Tschermak's substitution in antigorite
- and consequences for phase relations and water liberation in high-grade
- 1400 serpentinites. *Lithos*, *178*, 186-196.
- Raleigh, C. B., & Paterson, M. S. (1965). Experimental deformation of serpentinite and its
- tectonic implications. *Journal of Geophysical Research*, 70(16), 3965–3985.
- Reinen, L. A., Weeks, J. D., & Tullis, T. E. (1994). The frictional behavior of lizardite and
- antigorite serpentinites: Experiments, constitutive models, and implications for natural
- faults. Pure and Applied Geophysics, 143, 317–358.

Rutter, E. H. (1976). A discussion on natural strain and geological structure-the kinetics of 1406 1407 rock deformation by pressure solution. Philosophical Transactions of the Royal Society 1408 of London. Series A, Mathematical and Physical Sciences, 283(1312), 203–219. 1409 Scuderi, M. M., & Carpenter, B. M. (2022). Frictional stability and hydromechanical coupling of serpentinite-bearing fault gouge. *Geophysical Journal International*, 231(1), 290–305. 1410 Tajčmanová, L., Connolly, J. A. D. and Cesare, B. (2009), A thermodynamic model for 1411 titanium and ferric iron solution in biotite. Journal of Metamorphic Geology, 27: 153-1412 165. https://doi.org/10.1111/j.1525-1314.2009.00812.x 1413 Tarling, M. S., Smith, S. A. F., Scott, J. M., Rooney, J. S., Viti, C., & Gordon, K. C. (2019). The 1414 1415 internal structure and composition of a plate-boundary-scale serpentinite shear zone: 1416 the Livingstone Fault, New Zealand. Solid Earth, 10(4), 1025–1047. 1417 Tesei, T., Harbord, C. W. A., De Paola, N., Collettini, C., & Viti, C. (2018). Friction of 1418 Mineralogically Controlled Serpentinites and Implications for Fault Weakness. Journal 1419 of Geophysical Research: Solid Earth, 123(8), 6976–6991. 1420 https://doi.org/https://doi.org/10.1029/2018JB016058 Tulley, C. J., ten Thij, L., Niemeijer, A. R., Hamers, M. F., & Fagereng, Å. (2024). Activation of 1421 1422 dissolution-precipitation creep causes weakening and viscous behavior in experimentally deformed antigorite. Journal of Geophysical Research: Solid Earth, 1423 1424 129(8), e2024JB029053. White, R. W., Pomroy, N. E. and Powell, R. (2005), An in situ metatexite-diatexite transition 1425 1426 in upper amphibolite facies rocks from Broken Hill, Australia. Journal of Metamorphic 1427 Geology, 23: 579-602. https://doi.org/10.1111/j.1525-1314.2005.00597.x White, R. W., Powell, R., Holland, T. J. B., Johnson, T. E. and Green, E. C. R. (2014), New 1428 1429 mineral activity—composition relations for thermodynamic calculations in metapelitic systems. Journal of Metamorphic Geology, 32: 261-1430 286. https://doi.org/10.1111/jmg.12071 1431 White, R. W., Powell, R., Holland, T. J. B., & Worley, B. A. (2000). The effect of TiO2 and 1432 Fe2O3 on metapelitic assemblages at greenschist and amphibolite facies conditions: 1433 mineral equilibria calculations in the system K2O-FeO-MgO-Al2O3-SiO2-H2O-TiO2-1434

Fe2O3. Journal of Metamorphic Geology, 18(5), 497-511.

1435